Article

Unconventional Magnetization Generated from Electron Beam and Femtosecond Irradiation on α-Ag$_2$WO$_4$: A Quantum Chemical Investigation

Marcelo Assis, Renan Augusto Pontes Ribeiro, Maria Helena Carvalho, Mayara Mondego Teixeira, Yara Galvão Gobato, Gabriela Augusta Prando, Cleber Renato Mendonça, Leonardo de Boni, Adilson Jesus Aparecido de Oliveira, Jefferson Bettini, Juan Andrés,* and Elson Longo

Cite This: *ACS Omega* 2020, 5, 10052−10067
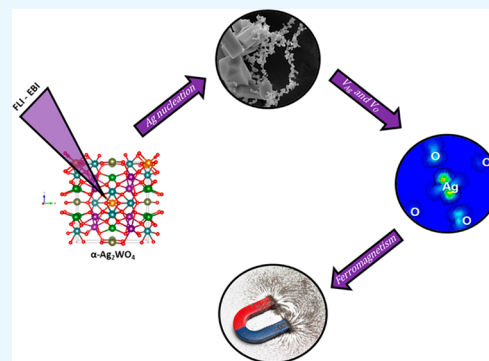
Read Online

ACCESS | Metrics & More | Article Recommendations | Supporting Information

ABSTRACT: Novel magnetic metals and metal oxides that use both the spin and charge of an electron offer exciting technological applications. Their discovery could boost research on functional nanoscale materials. Here, for the first time, we report the magnetization of α-Ag$_2$WO$_4$ under electron beam and femtosecond laser irradiation. The formation and growth of silver oxides (AgO, Ag$_2$O, and Ag$_3$O$_4$) and Ag nanofilaments can be observed on the surface of α-Ag$_2$WO$_4$ crystals. These features were also present in the composition of an extruded material and could open new avenues for surface magnetism studies. In order to understand these results, we used first-principles density functional theory calculations. This allowed us to investigate several potential scenarios for controlling magnetic properties. The effect of electron addition on the crystalline structures of α-Ag$_2$WO$_4$, Ag$_3$O$_4$, Ag$_2$O, and AgO has been analyzed in detail. The creation of Ag and O vacancies on these compounds was also analyzed. Based on structural and electronic changes at the local coordination site of Ag, a mechanism was proposed. The mechanism illustrates the processes responsible for the formation and growth of metallic Ag and the magnetic response to electron beam irradiation.

1. INTRODUCTION

Magnetic metals and metal oxides have attracted much attention over the past few decades because of their potential applications in spintronic devices. Atomic understanding, control, and prediction of their magnetic behavior is appealing because of their structural versatility and the accessibility of their low-energy spin exchange interactions. However, accomplishing this in a predictable manner has remained elusive and largely unexplored. A striking example is the observation of ferromagnetic-like behavior in nanomaterials which are otherwise diamagnetic (i.e., non-magnetic) in their bulk form,[1–3] such as Cu, Ag, and Au.[4–6] In particular, pure Ag, although diamagnetic in bulk states becomes magnetic at nanoscale. This behavior is linked to non-stoichiometric oxidation near the surface and does not show size dependency.[7] Ag displays an electronic valence configuration of $4d^{10}5s^1$, resulting in an overall magnetic moment in unbound atoms. This is due to the unpaired s electron in the Ag atom. As atoms form bulk materials; however, delocalization of the electronic states results in their well-known conductive and diamagnetic characteristics.[8,9] The display of multiple conductive behaviors can be attributed to a number of factors: (i) when chemically bound to oxide anions, Ag can adopt oxidation states that have unpaired d electrons; (ii) a variety of mechanisms can couple these unpaired d electrons, giving rise to collective behavior; and (iii) the relative ease with which these interactions can be modulated and tuned via chemical and structural modification.

It is well known that the observed ferromagnetism, at room temperature, originates from the oxygen vacancies for binary oxides such as HfO$_2$, CeO$_2$, Al$_2$O$_3$, ZnO, In$_2$O$_3$, SnO$_2$, TiO$_2$, and CuO.[3,10–19] The presence of neutral cation vacancies are responsible for the magnetic moment in MgO.[20–24] From a theoretical point of view, ab initio calculations have demonstrated that neutral cation vacancies are responsible for the magnetic moment in binary oxides such as CaO, HfO$_2$, TiO$_2$, ZnO, SnO$_2$, ZrO$_2$, and MgO.[25–34] The ferromagnetism in perovskites, like LiNbO$_3$ and LiTaO$_3$,[35] is associated with induced changes in the spin-polarized electronic structure of anion−cation interactions.[36]

Silver tungstate, Ag_2WO_4, is one of the most-promising silver-based materials because of its multifunctional properties across a wide range of fields. Its properties and uses include photoluminescence (PL), antibacterial, antitumor, lubricant, gas sensor, catalysis, light-emitting diode, and gate dielectrics.[37−47] The structural variability and broad technical applicability of Ag_2WO_4 are positive characteristics for realizing their structural and functional complexity. The top of the valence band (VB) consists of uniquely hybridized Ag 4d and O 2p orbitals. This can lift the top position of the VB, narrowing the bandgap. The bottom of the conductance band (CB), consisting of delocalized s and/or p orbitals, displays significant dispersity. As a result, photogenerated electrons show high migration efficiencies.[48,49]

There has been extensive work on the synthesis and characterization of atomically precise Ag nanoclusters with unusual properties.[50,51] Our research group recently used transmission electron microscopy (TEM) and scanning electron microscopy (SEM) to demonstrate that electron beam irradiation (EBI) on α-Ag_2WO_4 creates an opportunity for the formation of Ag nanoparticles (Ag NPs) under high vacuum at room temperature. EBI also allows the growth of Ag NPs to be manipulated as they emerge from the surface of different Ag-based materials, such as Ag_2WO_4,[52−54] Ag_2MoO_4,[55,56] and Ag_3PO_4 crystals.[57] Additionally, we have used femtosecond laser irradiation (FLI) on α-Ag_2WO_4 to scale-up the formation of bactericidal Ag NPs.[58] According to our experimental and theoretical results, both EBI and FLI excite the electron−lattice system, modifying atomic structures and inducing the reduction of Ag cations in the corresponding lattice. Therefore, the unique electron/wave−matter interactions with materials are an appropriate tool for forming NPs from the bulk structures.

EBI and FLI cause structural distortions. These originate from oxygen and cation vacancies, strong cation−anion−cation interactions, and the associated influence on the stability of the Ag cation valence states. This has a dramatic effect on the local order. EBI and FLI both excite the electron−lattice system. This modifies the atomic structures and induces the reduction of Ag cations. High-resolution TEM (HR-TEM) images taken by our group revealed that in addition to cubic metallic Ag NP formation from EBI on α-Ag_2WO_4, cubic (Ag_2O) and monoclinic (Ag_3O_4) silver oxides were also present.[59] Considering these observations and the non-magnetic nature of α-Ag_2WO_4, the next focus of our research was to provide reasonable explanations for the observations and to then answer the following questions: is it possible for magnetism to be induced by EBI or FLI on α-Ag_2WO_4? What is the mechanism for the magnetism response from binary oxides of Ag_2O, Ag_3O_4, and AgO?
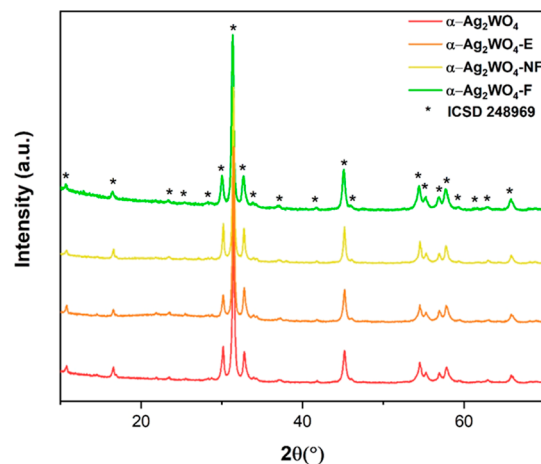
We carried out experimental and theoretical investigations based on density functional theory (DFT) calculations to gain a deep understanding of the magnetic behavior in α-Ag_2WO_4, Ag_2O, Ag_3O_4, and AgO. We also explored the role EBI and FLI play in the creation of defects, such as Ag and O vacancies. The aforementioned vacancies and local spins are two major factors affecting the induction of magnetism in these Ag-based materials. They offer new opportunities for nanomagnetism and surface magnetism.

This paper contains an additional three sections. The next section is the Experimental Section where the synthesis, characterization, computational methods, and model systems are discussed. Section three offers presentation and discussion

of the results. Conclusions are summarized in the final fourth section.

2. RESULTS AND DISCUSSION

2.1. X-ray Diffraction. Figure 1 shows the X-ray diffraction (XRD) patterns for the synthesized α-Ag_2WO_4 sample, the

Figure 1. XRD patterns for the samples of α-Ag_2WO_4.

FLI-modified focused and non-focused samples (α-Ag_2WO_4:F and α-Ag_2WO_4:NF, respectively), and the EBI sample (α-Ag_2WO_4:E). XRD analysis was performed to demonstrate order and disorder at long ranges. In addition to showing the periodicity and organization of the crystalline lattice, the XRD patterns show the unit cell structures. All samples have well-defined diffraction peaks, indicating a good degree of structural order in the crystalline lattice at long-range. All α-Ag_2WO_4 samples had an orthorhombic structure and $Pn2n$ spatial group, according to card no. 248969[60] in the Inorganic Crystal Structure Database (ICSD). This phase was composed of distorted-octahedral clusters of $[WO_6]$ and angular, tetrahedral, octahedral, and distorted-deltahedral clusters $[AgO_x,$ where x = 2, 4, 6, and 7], with lattice parameters a = 10.878 Å, b = 12.009 Å, c = 5.895 Å, α = β = γ = 90°. There were no observed differences between the various α-Ag_2WO_4 samples in the diffractograms. Additionally, there was no presence of a second phase. This can be explained by the fact that the formation of $Ag^{52,58}$ and Ag_yO_x[59] NPs occurs on the surface of FTI and EBI materials. This is due to the reduction of Ag (localized in some clusters of the material). The reduction creates new nAg/α-$Ag_{1−n}WO_4$ interfaces, nAg_xO_y/α-$Ag_{1−n}WO_4$ interfaces, and silver vacancies inside the crystal.

The Rietveld refinement method was employed to show differences in the phase compositions and structural compositions of α-Ag_2WO_4 samples. For this analysis, the refined parameters were the scale factor, background, shift lattice constants, profile half-width parameters (u, v, w), isotropic thermal parameters, lattice parameters, strain anisotropy factor, preferred orientation, and atomic functional positions.[61−63] Table 1 shows the parameters obtained from the Rietveld refinements of α-Ag_2WO_4 samples. The statistic fitting parameters (GOF and R_{wp}) indicate that the quality of the structural refinement data is acceptable (Figure S1).

The Rietveld refinements show that the irradiations interfered with the structural order of the $[WO_6]$ and $[AgO_x]$ clusters (constituent building blocks of the α-

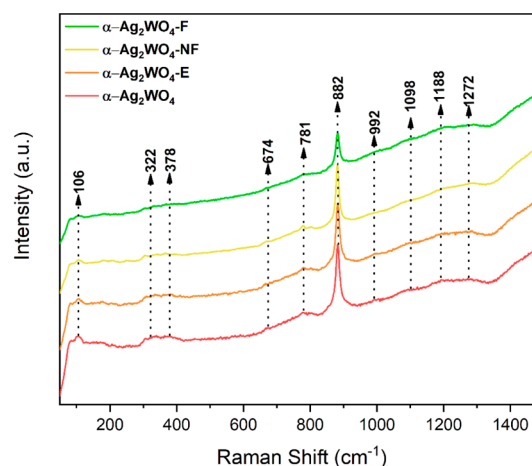**Table 1. Results Obtained from Rietveld Refinements of α-Ag$_2$WO$_4$ Samples**

sample	a (Å)	b (Å)	c (Å)	V (Å^3)	fwhm (deg)	GOF	R_{wp} (%)
α-Ag$_2$WO$_4$	10.85	11.99	5.88	766.07	0.25	2.01	8.3
α-Ag$_2$WO$_4$:E	10.87	12.06	5.91	774.16	0.27	2.00	8.4
α-Ag$_2$WO$_4$:NF	10.87	12.04	5.89	773.46	0.27	1.45	8.7
α-Ag$_2$WO$_4$:F	10.94	12.11	5.94	787.07	0.35	1.69	9.3

Ag$_2$WO$_4$ samples) at short-distances. The EBI and FLI samples suffered an increase in the values of the a, b, and c lattice parameters. This caused an increase in the crystalline cell volume of α-Ag$_2$WO$_4$.

It can be observed that although the diffractograms do not present differences to the naked eye, the Rietveld refinements show that the irradiations interfered with the structural order of the [WO$_6$] and [AgO$_x$] clusters (constituent building blocks of the α-Ag$_2$WO$_4$ samples) at short-distance. The EBI and FLI samples suffered an increase in the values of the a, b, and c lattice parameters. This caused an increase in the crystalline cell volume of α-Ag$_2$WO$_4$. This phenomenon occurs due to expansion of the crystalline lattice. This effect can be associated with a reduction in the size of the Ag clusters ([AgO$_x$], where x = 2, 4, 6, and 7) due to EBI and/or FLI-induced formation of the metallic Ag and Ag$_x$O$_y$ species.[58,59] These changes can be related to the full width at half maximum (fwhm) of the main crystallographic peak [231] in $2\theta = 32°$ of α-Ag$_2$WO$_4$. This is because increases in these values are associated with a higher structural disorder of the crystalline system of the samples. These disorders are more pronounced in the α-Ag$_2$WO$_4$:F sample because its photon concentration occurs in a very small area. This causes a greater damage to the sample, compared to the α-Ag$_2$WO$_4$:NF and α-Ag$_2$WO$_4$:E samples.

2.2. Micro-Raman Spectroscopy. Micro-Raman spectroscopy is an important technique for understanding the effects of structural order/disorder on crystalline solids at short ranges. For a crystal without defects, the Raman spectrum must obey the selection rules and should be composed of lines, which correspond to the central point of the allowed zone. According to group theory analysis, the allowed representation for each of the corresponding Wyckoff positions of the orthorhombic structure of α-Ag$_2$WO$_4$ (symmetry group C_{2v}^{10}) indicates 21 active Raman modes corresponding to decomposition at the $\Gamma = (6A_{1g} + 5A_{2g} + 5B_{1g} + 5B_{2g})$ point.[58,64] Out of these 21 modes for the range of micro-Raman scattering spectra studied, 10 were identified, as shown in Figure 2.
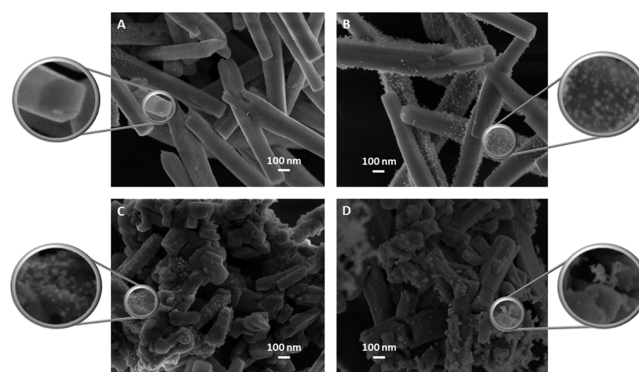
The most intense band, at 882 cm^{-1}, refers to the symmetrical stretching of [WO$_6$] octahedral clusters, relative to the A_{1g} mode.[65,66] There is an active mode in the spectral region of 781 cm^{-1}, corresponding to the asymmetrical stretching of the [WO$_6$] clusters (the B_{1g} mode).[65,66] Only one mode was observed in the 500–700 cm^{-1} region. This appears at 674 cm^{-1}, relative to the B_{1g} mode.[65] Between 150 and 400 cm^{-1}, two bands are present: one at 322 cm^{-1}, and the other at 378 cm^{-1} relative to the A_{2g} modes that were attributed to vibrations in the [AgO$_x$] (x = 2, 4, 6, and 7) clusters.[66] Finally, a 106 cm^{-1} mode is observed, which represents a B_{1g} transition in the crystal lattice modes of Ag.[64] The predicted and unobserved modes in the materials are associated with high disorder at short distances from the samples. An A_{1g} mode is not observed because its band appears in a lower wavelength region (<50 cm^{-1}).[65] Furthermore, the α-Ag$_2$WO$_4$–F sample showed less-defined modes than the α-

Figure 2. Micro-Raman spectra for the samples of α-Ag$_2$WO$_4$.

Ag$_2$WO$_4$ sample. This indicates that FLI in the focused mode increased short-range disorders in the sample's [WO$_6$] clusters, [AgO$_x$] clusters, and Ag vacancies.

2.3. Scanning Electron Microscopy (SEM). SEM is essential for the determination of shape, texture, topography, and surface features. Synthesis conditions, such as temperature, pressure, pH, and solvent, can cause morphological modifications in the sample material. Modification can also be caused by sources or irradiation, such as EBI and FLI, or chemical reactions, such as acidic and basic attacks.

The morphology of α-Ag$_2$WO$_4$ samples (Figure 3A) were rod-like with hexagonal shape and [001], [010], and [101]

Figure 3. SEM images for the samples (a) α-Ag$_2$WO$_4$; (b) α-Ag$_2$WO$_4$:E; (c) α-Ag$_2$WO$_4$:NF; and (d) α-Ag$_2$WO$_4$:F.

surfaces,[66,67] as shown in the inset of the images. When α-Ag$_2$WO$_4$ is irradiated by electrons, the formation of nanofilaments on the material surface become more pronounced (Figure 3B), as reported by our research group.[66] This is due to reduction of the atomic charge located in the [AgO$_2$] and [AgO$_4$] clusters of α-Ag$_2$WO$_4$, which causes the reduction of Ag^{+1} to Ag^0, creating clusters with V$_{Ag}$.[68,69] The diffusion of Ag and O atoms in the system can still occur, giving rise to Ag$_x$O$_y$
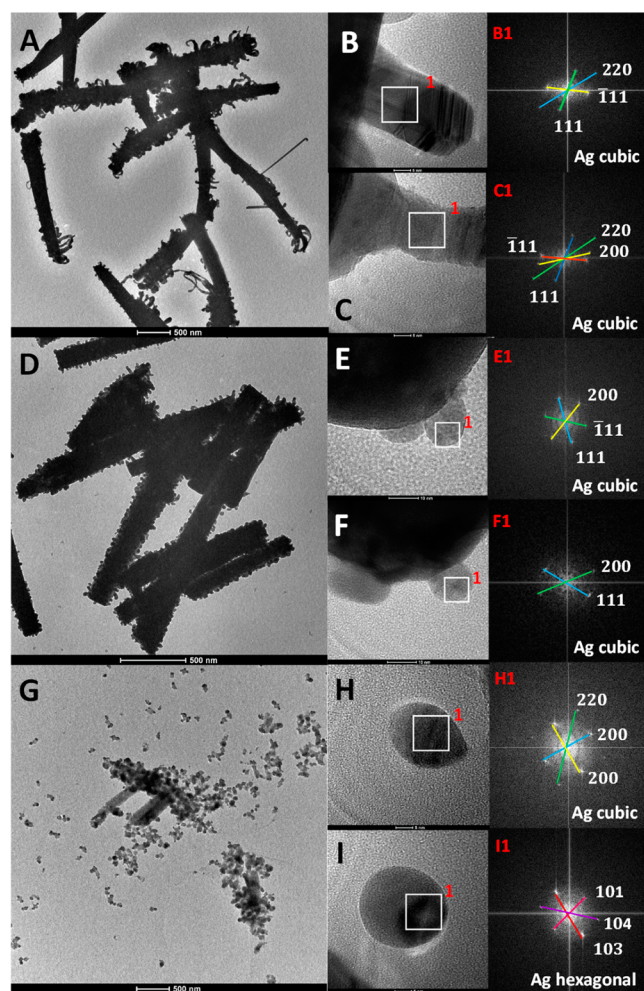
species in this process.[59] Thus, α-Ag$_2$WO$_4$, an n-type conductor, becomes a semiconductor with randomly distributed n/p quantum dots. Coalescence of the rods and formation of spheroidal particles are observed when the semiconductor is irradiated with fs laser (Figure 3C,D).This happens because FLI of α-Ag$_2$WO$_4$ induces a photoactivation process involving multiphotonic absorption of an electron. The excited electrons are capable of transferring energy to the crystalline lattice of α-Ag$_2$WO$_4$. The α-Ag$_2$WO$_4$ lattice can sinter or cause a high formation of Ag^0 on the surface of the semiconductor.[58] This effect is more evident in the α-Ag$_2$WO$_4$:F sample (Figure 3D) due to the larger concentration of photons per cm^2. Like the effect caused by electrons, the semiconductor presents p-character due to the formation of V$_{Ag}$ in α-Ag$_2$WO$_4$.

2.4. Transmission Electron Microscopy. TEM analysis for samples α-Ag$_2$WO$_4$:E, α-Ag$_2$WO$_4$:NF, and α-Ag$_2$WO$_4$:F was performed in order to investigate the species formed after EBI and FLI and are shown in Figure 4. Figure 4A shows the results for the α-Ag$_2$WO$_4$:E sample. In contrast to SEM images, there is an increase in Ag nanofilaments because the acceleration energy used in TEM (200 kV) is higher than in SEM (15 kV). HR-TEM images (Figure 4B,C) show that the filaments are composed of cubic Ag^{70} (fast Fourier transform

(FFT)—Figure 4B1−C1), indicated by the planes [111], [$\bar{1}$11], [200], and [220], as already observed in previous studies.[42,43,45] Similarly, for sample α-Ag$_2$WO$_4$:NF (Figure 4D), it was observed that the spheroid particles associated with the α-Ag$_2$WO$_4$ rods (Figure 4E,F) are also formed of cubic Ag^{70} (FFT—Figure 4E1−F1), indicated also by the planes [111], [$\bar{1}$11], and [200].[38,58] Because of the higher concentration of photons per cm^2, for the sample α-Ag$_2$WO$_4$:F (Figure 4G), there is a disruption of the initial morphology, with the formation of spheroidal particles disassociated from the rods (Figure 4H,I). It is observed that these particles are formed by cubic Ag^{70} (FFT—Figure 4H1), indicated by the presence of planes [200] and [220], and hexagonal Ag^{71} (FFT—Figure 4I1), with presence of the planes [101], [103], and [104] as already reported by our research group.[72] The hexagonal Ag phase, despite being a metastable polymorph of Ag, can be found distributed in natural and artificial sources of Ag.[73,74] Because of the high energy from FLI, stabilization of metastable phases can occur, as already observed for polymorphs of Ag and Bi.[72,75]
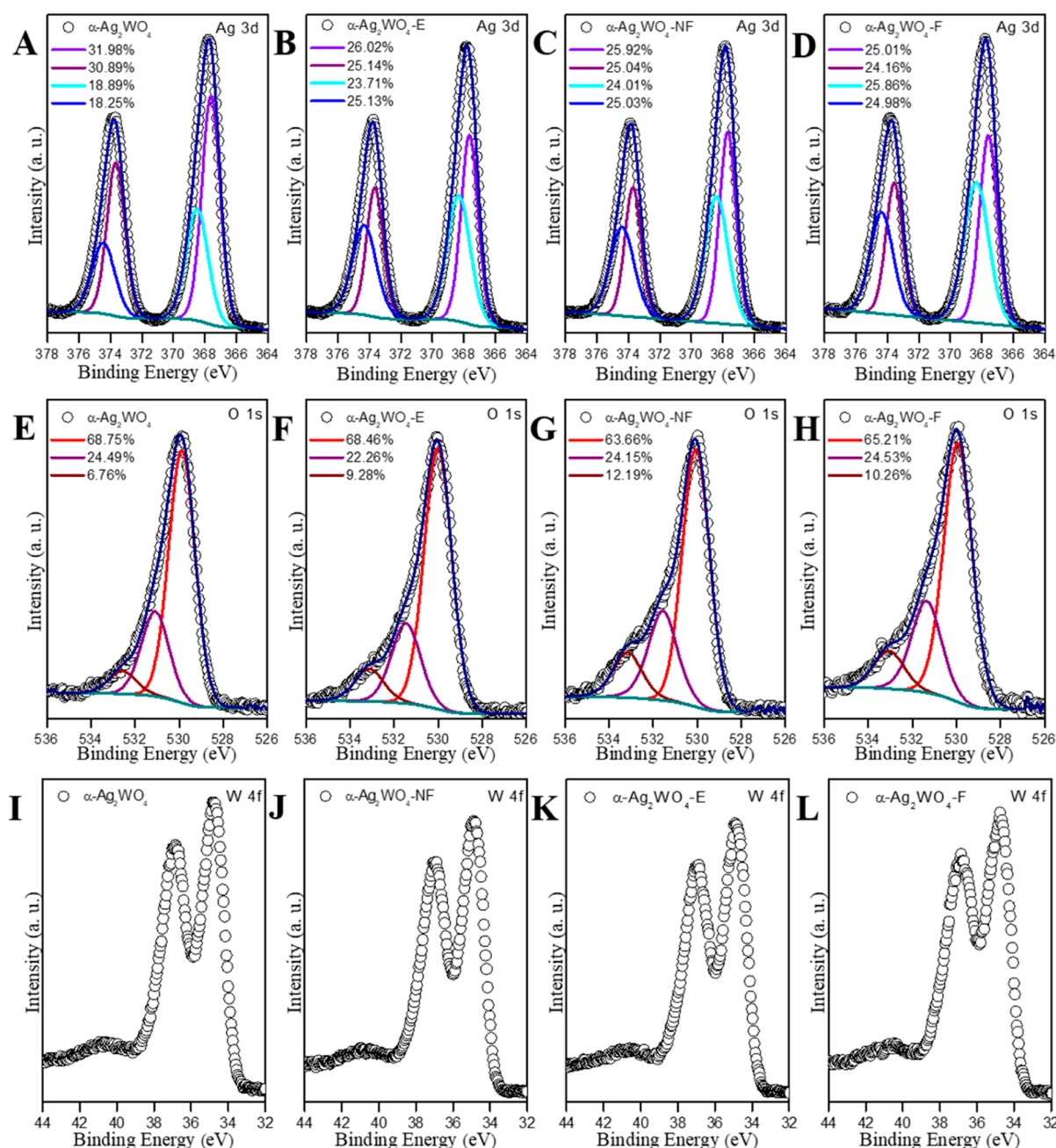
It was not possible to observe the formation of Ag-based oxides in these micrographs; however, according to Sczancoski et al.,[59] they are located at the α-Ag$_2$WO$_4$/Ag interface. When Ag structures are formed with EBI, a diffusional movement of Ag and O atoms from inside to outside the α-Ag$_2$WO$_4$ rods occurs. The Ag atoms are able to diffuse more, forming metallic structures, and the O atoms are located at the α-Ag$_2$WO$_4$/Ag interface, forming these Ag-based oxides.[59] We believe that it was not possible to identify these species in these micrographs, as the resolution of the observed interfaces is not clear, making this identification impossible. It is important to detach that the non-identification of the formation of these Ag-based oxides,[59] already evidenced in another work by a group,[59] is not ruled out.

2.5. X-ray Photoelectron Spectroscopy. X-ray photo-electron spectroscopy (XPS) analysis was performed in order to evaluate the sample chemical compositions and surface valence states. Figure S2 shows the survey spectra of the α-Ag$_2$WO$_4$ samples. The presence of the main binding-energy peaks of Ag, W, and O atoms were observed in all the samples. The C peaks were also observed because the sample ports from the XPS instrument. Figures 5A−D shows high-resolution XPS spectra of the 3d region of Ag in the α-Ag$_2$WO$_4$ samples. The peaks at ~374 and ~368 eV are associated with the Ag 3d$_{3/2}$ and Ag 3d$_{5/2}$ doublet binding energies, respectively. Moreover, each of these peaks could be fit into two separate components. This indicates that different oxidation states of Ag were present, creating the possibility of unpaired electrons, inducing the system magnetic property when irradiated. The components at 374.8 and 368.8 eV are related to Ag^0, and the ones at 373.9 and 367.8 eV can be assigned to Ag$^+$.[76] The percentages of Ag^0 on the surface of the α-Ag$_2$WO$_4$ samples were 37.14, 51.16, 50.96, and 50.84% for α-Ag$_2$WO$_4$, α-Ag$_2$WO$_4$:E, α-Ag$_2$WO$_4$:NF, and α-Ag$_2$WO$_4$:F, respectively. In agreement with Assis et al.,[38] we observed an increased tendency for the formation of metallic Ag in the EBI and FLI-treated α-Ag$_2$WO$_4$ samples. The concentration of Ag^0 in the α-Ag$_2$WO$_4$ sample was due to interactions between the XPS X-ray and the sample. Figure 5E−H shows high-resolution XPS spectra for O atoms in the samples of α-Ag$_2$WO$_4$. The O 1s peak was fit into three separate components with binding energies of 533.1, 531.9, and 530.8 eV. These were assigned to the chemisorbed oxygen, the defect oxygen, and the oxygen lattice, respectively.[77] Figure

Figure 4. TEM images of α-Ag$_2$WO$_4$ composites of exposure to a 200 kV electron beam. (A−C) α-Ag$_2$WO$_4$:E; (D−F) α-Ag$_2$WO$_4$:NF; and (G−I) α-Ag$_2$WO$_4$:F.
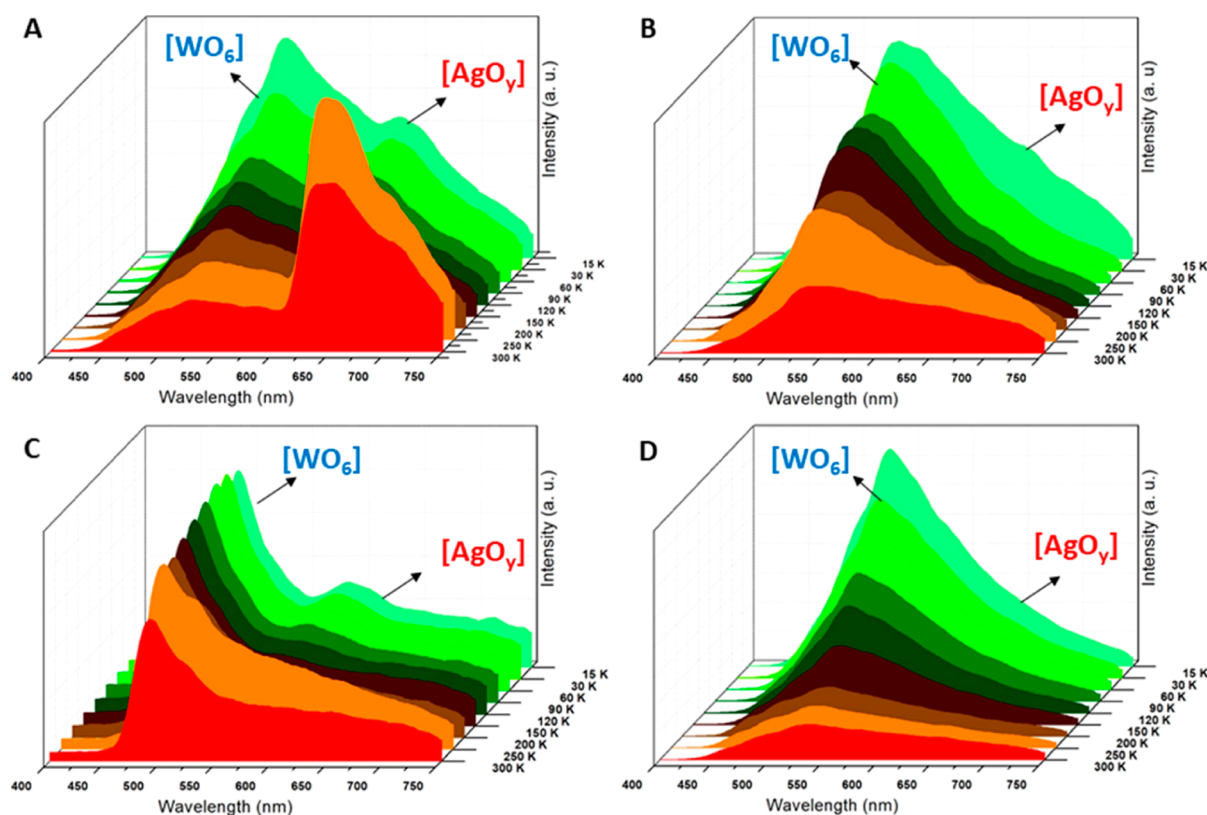
Figure 5. (A−D) XPS spectra of Ag 3d, (E−H) O 1s, and (I−L) W 4f for α-Ag$_2$WO$_4$, α-Ag$_2$WO$_4$:E, α-Ag$_2$WO$_4$:NF, and α-Ag$_2$WO$_4$:F, respectively.

5I−L shows high-resolution XPS spectra for the W^{6+} ions in the WO_4^{2-} of the samples. The two components have binding energies of 36.6 eV (assigned to W 4f$_{7/2}$) and 34.4 eV (W 4f$_{5/2}$).[77,78]
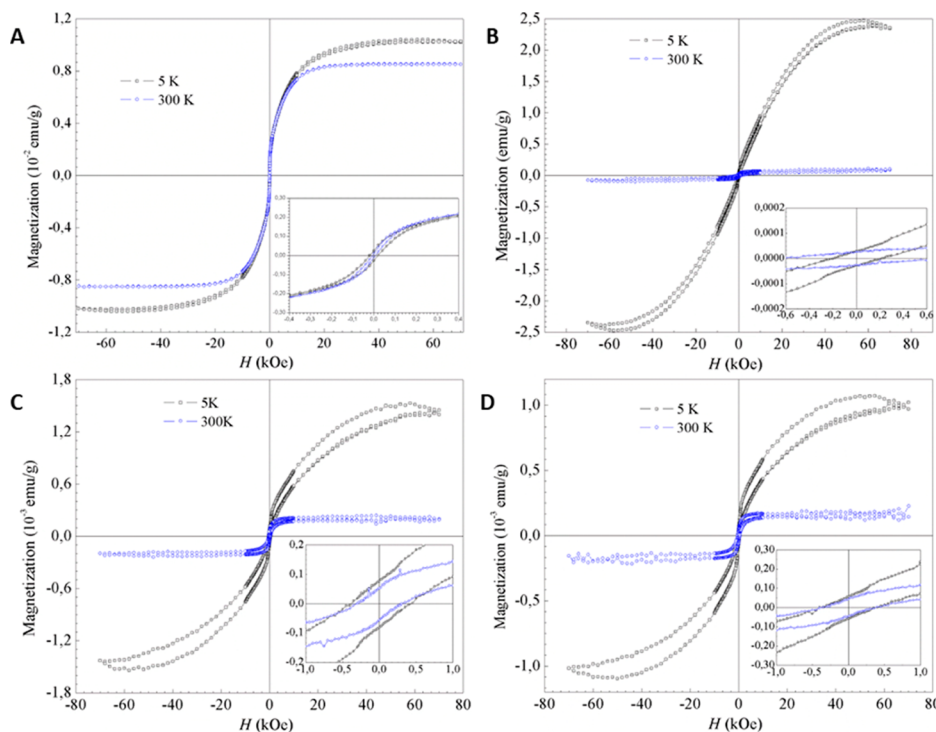
2.6. PL Emissions. Figure 6 shows the PL spectra for all the α-Ag$_2$WO$_4$ samples. Measurements were taken as a function of temperature (15−300 K) with laser excitation at 325 nm. The PL spectra indicate multiphonon processes where, with the participation of various intermediary states within the forbidden band gap region, relaxation occurs by multiple pathways.[79,80] The PL spectra of the α-Ag$_2$WO$_4$ come from the [WO$_6$] octahedral clusters and the [AgO$_x$] (x = 2, 4, 6, and 7). Maximum emissions were found in the blue-green and red regions, respectively (Figure 6A).[1,52,66,67] PL emission in the blue-green region is associated with charge transitions in the [WO$_6$] octahedral cluster (ground state $^1A_1$ to the high $^1T_2$

vibration level).[81,82] The mechanism of luminescence is determined by the charge transfer within the [WO$_6$] clusters. This involves the 2p orbital of O anions, the 4d orbital of Ag cations in the VB, and the 5d orbital in the W cation in the CB.[60] Moreover, it is known that modified lattices, for example, lattices with increased structural defects, also favor emission in the more-energetic blue-green region.[61,83]

For the α-Ag$_2$WO$_4$ sample (Figure 6A), PL emissions show a strong peak in the blue-green region at low temperature. This peak at 532 nm (2.33 eV) has been assigned to the transition in the [WO$_6$] clusters. With increasing temperature, the transition in the red region is strongly favored at 636 nm (1.95 eV). Increasing the temperature enhances the electron−phonon interaction in the semiconductor, and the electron undergoes a non-radiative decay from the higher energy level (2.33 eV) of the CB to the lower energy level (1.95 eV)

Figure 6. Temperature dependence of PL spectra for (A) α-Ag$_2$WO$_4$; (B) α-Ag$_2$WO$_4$:E (C) α-Ag$_2$WO$_4$:NF; and (D) α-Ag$_2$WO$_4$:F under excitation at 325 nm.

Figure 7. Magnetization as a function of applied magnetic field ($M \times H$) at 5 and 300 K. The inset shows details of low-field region samples (A) α-Ag$_2$WO$_4$; (B) α-Ag$_2$WO$_4$:E; (C) α-Ag$_2$WO$_4$:NF; and (D) α-Ag$_2$WO4:F. The diamagnetic contribution was subtracted from all measurements using a linear fitting in high-field regime.

located in the band gap. In non-radiative decay, the energy is transferred to the lattice by means of vibrations and heating. Subsequently, there is radioactive decay with photon emission.

This appears in the red region, corresponding to lower energy of longer wavelength. For the EBI and FLI samples (Figure 6B–D), the emission in the blue-green region appears at 544

Figure 8. Magnetization as a function of temperature ($M \times T$) performed at 10 kOe using the ZFC/FW procedure (A) α-Ag_2WO_4; (B) α-Ag_2WO_4:E; (C) α-Ag_2WO_4:NF; and (D) α-Ag_2WO_4:F. The diamagnetic contribution was subtracted from all measurements using a linear fitting in high-field regime, obtained from $M \times H$ measurements.

nm (2.28 eV) for α-Ag_2WO_4:E, 490 nm (2.53 eV) for α-Ag_2WO_4:NF, and 532 nm (2.33 eV) for α-Ag_2WO_4:F. This is true even when temperature is varied from 15 to 300 K. The emission at high energies may be strongly influenced by structural defects in the lattice. This transition comes from $[WO_6]$ clusters. It is also due to the presence of surface defects in the irradiated samples. Both long and short-range structural disorder was observed in irradiated samples causing high structural disorder in the samples, as shown in the XRD and Raman spectra. Additionally, for the samples modified with EBI (Figure 6B) and FLI (Figure 6C,D), a decrease in the intensity of emission in the red region can be seen. This can be explained by the fact that when α-Ag_2WO_4 is treated with EBI and FLI, more-severe modifications occur directly in the $[AgO_x]$ clusters (x = 2, 4, 6, and 7). This is due to the reduction of Ag cations and/or the formation of Ag-based oxides. Thus, the electron density generated by a large amount of V_O in the $[AgO_x]$ clusters can recombine with the V_{Ag} generated in α-Ag_2WO_4, resulting in a decrease in the PL emissions at the red region.
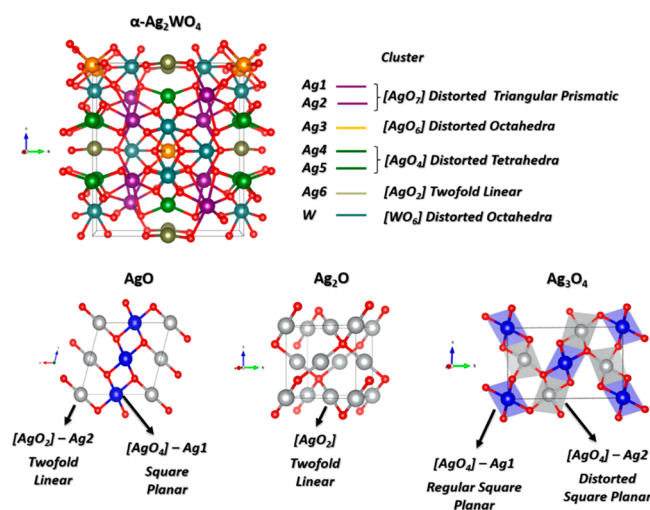
2.7. Magnetic Measurements. Figure 7 shows magnetization measurements for (a) α-Ag_2WO_4; (b) α-Ag_2WO_4:E; (c) α-Ag_2WO_4:NF; and (d) α-Ag_2WO_4:F. The measurements were performed up to 300 K as a function of the applied magnetic field. From Figure 7A, we observe that paramagnetic behavior and coercive field are not at low and high temperatures. This behavior is confirmed by the results displayed in Figure 7A, where Curie−Weiss behavior was observed across the full temperature range. On the other hand, analysis of Figure 7B−D shows that all samples exhibit ferromagnetic behavior in the range of 5−300 K. This is characterized by remnant magnetization ($\sim 1.0 \times 10^{-4}$ emu/g)

and coercive field ($\sim$500 Oe). At low temperature, the paramagnetic behavior overlaps with ferromagnetic contribution due to the presence of non-interacting magnetic moments.

Figure 8B−D shows that $M \times T$ increased due to paramagnetic contribution at low temperatures. In contrast, $M \times T$ decreased at high temperatures, as expected for ferromagnetic systems. This unusual behavior could also be associated with the presence of both non-interacting magnetic moments (paramagnetic contribution) and ordered magnetic moments (ferromagnetic contribution). The coexistence of the two magnetic trends (due to the presence the two aforementioned types of magnetic moments) will be investigated using DFT results.

Under EBI and FLI α-Ag_2WO_4 presents magnetic properties. This is initially surprising, but it creates new prospects for nanomagnetism and surface magnetism. V_{Ag}, V_O, and local spins are major factors affecting the induction of magnetism in these Ag-based materials. As multiferroic materials, these defective metal oxides are of great interest and present opportunities for various domains of research. This behavior can be explained by the cation off-centering mechanism for ferroelectrics (which generally requires d^0 orbitals) and the formation of magnetic moments (which usually results from partially filled d orbitals).

2.8. DFT Calculations. The optimized structures of α-Ag_2WO_4, Ag_3O_4, Ag_2O, and AgO oxides are presented in Figure 9. Analysis of the geometries show a wide range of clusters corresponding to the local coordination of Ag cations, that is, Ag-centered clusters with distinct coordination numbers $[AgO_x]$ (x = 2, 4, 6, and 7) and chemical environments that provide different sites for electron-induced reduction and creation of V_{Ag} sites. This phenomenon requires

Figure 9. Crystallographic unit cell of α-Ag_2WO_4, Ag_3O_4, Ag_2O, and AgO oxides. The constituent clusters, i.e., local coordination of the Ag cation is depicted for each system.
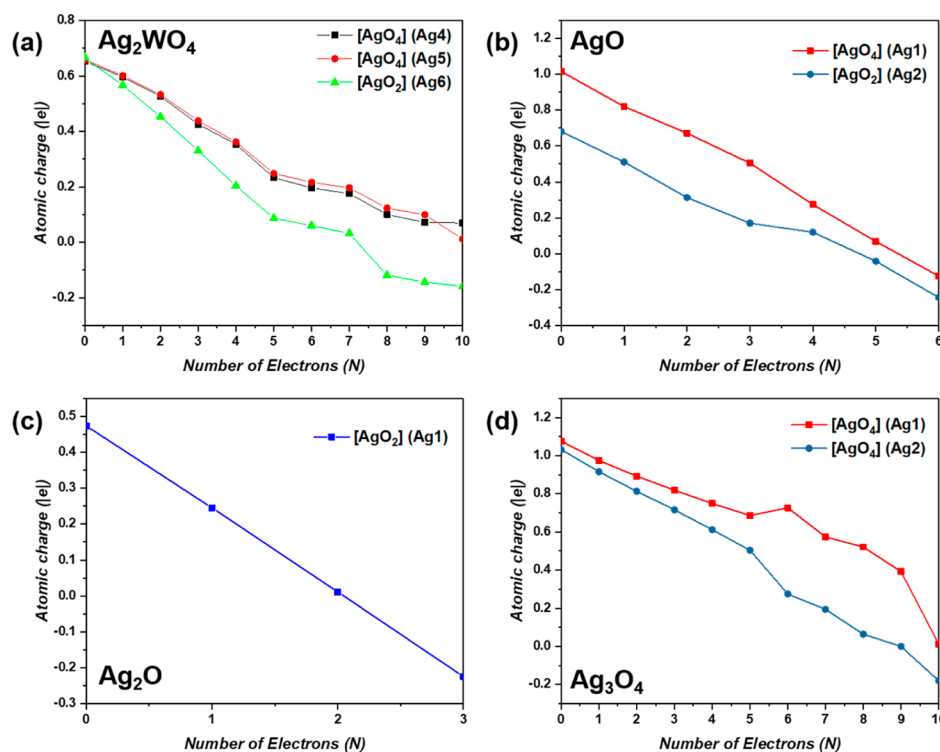
deeper investigation into the local effects and the mechanism associated with the EBI.

To this end, we have carried out a systematic theoretical study based on DFT + U calculations with consideration to electron addition inside the crystalline structure of Ag-based oxides. The structural changes were analyzed, and the electronic evolution has been investigated using Bader charge analysis within the QTAIM framework. Figure 10 depicts the Bader atomic charge of Ag, W, and O centers as a function of the number of electrons added to the system (N).

The results in Figure 10A highlight that the two-fold $[Ag_2O]$ cluster of α-Ag_2WO_4 is the most favorable site for the
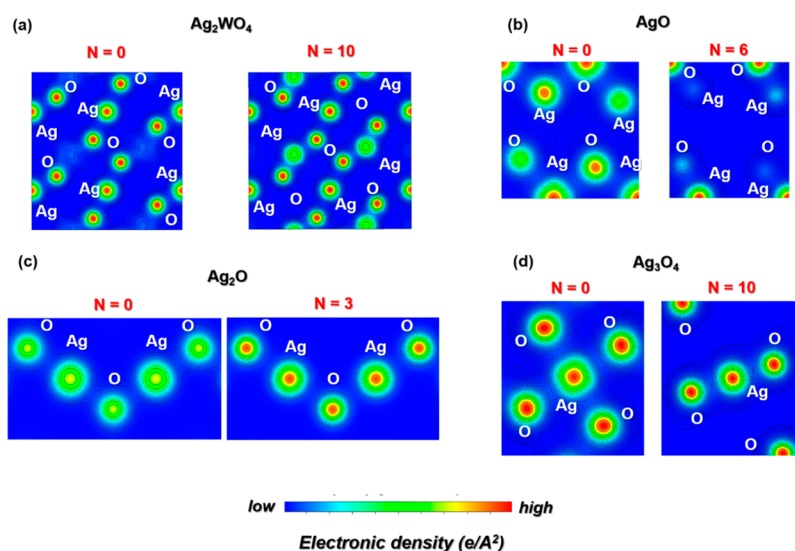
reduction of the Ag species (responsible for growth of Ag NPs). Moreover, the bond distances summarized in Figure S3 indicate that the Ag–O bond distances in the $[Ag_2O]$ cluster increase with N. This is associated with the Ag–O bond-breaking process and concomitant reduction of the Bader charge of the Ag center. This is followed by an enlargement of two bonds in the $[Ag_4O]$ clusters. These become $[Ag_2O]$ after electron addition. Similar behaviors have been discussed in previous studies, where a mechanism for the electron-induced growth of metallic NPs has been resolved.[56,68,75] In addition, electron density maps were plotted in order to describe this effect, as presented in Figure 11. This result can be interpreted by the sharing of isolines between the atomic centers that indicates an accumulation of electron density along the bond path describing the existence of chemical bonds. On the contrary, the bond breaking mechanism can be attributed to the differential map where the isolines are not shared between neighboring atoms, and it is usually related to the concentration of electron density at the atomic centers.

The contour plot in Figure 11A indicates the formation of $[Ag_4O]$ in the α-Ag_2WO_4 material at $N = 0$; while the density map at $N = 10$ is the result of the bond-breaking mechanism responsible for creating $[Ag_2O]$ clusters after electron addition. The results presented in Figures 10B–D and 11B–D show similar behaviors in other Ag-based oxides. For AgO oxide (Figure 10B), the crystalline structure contains two different Ag sites: square planar $[AgO_4]$ cluster with a low-spin non-magnetic Ag^{3+} $(4d^8)$ cations, while the two-fold $[AgO_2]$ clusters are centered at Ag^{1+} $(4d^{10})$ cations. The obtained results, as a function of N, indicate that the Ag in the $[AgO_2]$ clusters are the most labile sites for reduction and formation of metallic Ag. This is followed by the charge reduction of Ag^{3+} in the $[AgO_4]$ cluster. Indeed, the bond lengths in $[AgO_4]$

Figure 10. Bader atomic charges for Ag centers as function of the number of electrons added to the system (N) for (a) α-Ag_2WO_4, (b) AgO, (c) Ag_2O, and (d) Ag_3O_4.
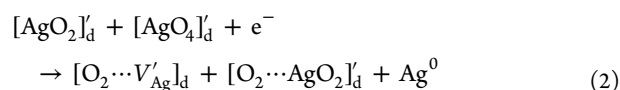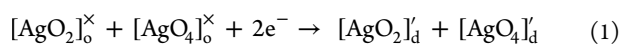
Figure 11. Electron density contour plots for a neutral ($N = 0$) structure and a charged ($N \neq 0$) structure for (a) α-Ag_2WO_4, (b) AgO, (c) Ag_2O, and (d) Ag_3O_4.

(Figure S3) suggest that reduction is followed by a structural distortion that modifies the chemical environment for this site prior to becoming a two-fold $[AgO_2]$ cluster. This is the subsequent site for generation of reduced Ag species (see Figure 11B). The addition of electrons, and subsequent formation of metallic silver, leads to the generation of V_{Ag}, randomly forming p-type quantum dots, in the n-type semiconductor.

Results for Ag_2O (see Figure 10B) suggest that large structural distortions in the $[AgO_2]$ clusters accompany the reduction of Ag and the generation of metallic Ag centers. This may be associated with the structural displacement of Ag cations during formation of the crystalline structure of metallic Ag (see Figure 11C). This is in agreement with previous research.[52,56,68,75] Let us now briefly discuss the mechanism associated with the Ag_3O_4 system (see Figure 10C), where distorted $[AgO_4]$ clusters are the most favorable site for charge reduction and generation of metallic Ag centers. The regular $[AgO_4]$ becomes distorted as N is increased. The associated redistribution of electronic density causes local structural disorder (see Figure 11D).

From the above results, we can propose a general mechanism for charge reduction and the generation of metallic Ag centers. These are based on the equation of defects associated with the Kröger−Vink notation.[84] In this formalism, the mechanism of electron charge addition can be described using the neutral $[AgO_n]^{\times}$ and negatively charged $[AgO_n]'$ cluster notation, and the following charge-transfer mechanism can be proposed

$$[AgO_2]_o^{\times} + [AgO_4]_o^{\times} + 2e^- \rightarrow [AgO_2]_d' + [AgO_4]_d' \quad (1)$$

$$[AgO_2]_d' + [AgO_4]_d' + e^-$$
$$\rightarrow [O_2{\cdots}V_{Ag}']_d + [O_2{\cdots}AgO_2]_d' + Ag^0 \quad (2)$$
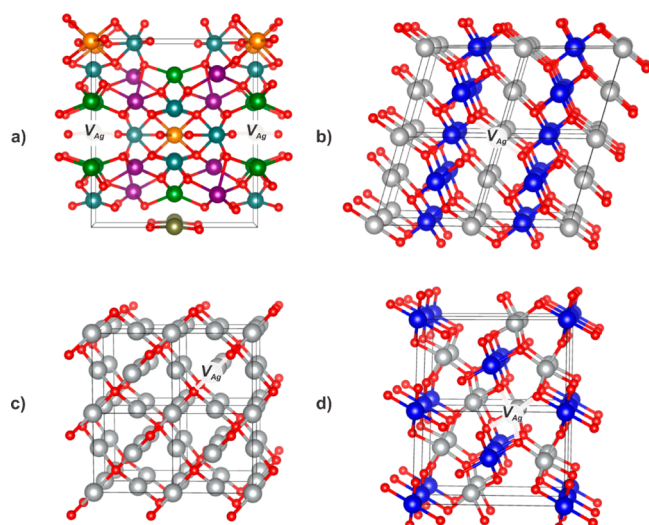
where o = ordered and d = disordered.

The first step of the mechanism is the transformation of regular (ordered) $[AgO_2]$ and $[AgO_4]$ clusters in the Ag-based oxides. This is induced by the addition of electrons, leading to the generation of distorted (disordered) $[AgO_2]$ and $[AgO_4]$ clusters. In the following step, the distorted clusters interact

with negative charges. As a result, the Ag centers are reduced, and there is formation of V_{Ag}. This is accompanied by structural distortion of the remaining $[AgO_4]$ cluster which becomes $[AgO_2]$. In the final step, the addition of new electrons induces the formation of metallic Ag^0 species through a vacant site in the crystalline structure of Ag-based oxides. The growth of metallic Ag NPs is increased by structural distortion of neighboring $[AgO_4]$ clusters. In this way, the effect is transferred along the crystal lattice.

DFT calculations were performed to describe the main role of V_{Ag} in the electronic structures associated with the generation of electronic holes at the vacant site. This offered a better understanding of the mechanism associated with the electron-induced formation of V_{Ag} centers in the Ag-based oxides. In this case, we consider the creation of V_{Ag} centers based on calculations that indicate the most favorable sites for electron-beam induced reduction of Ag centers, as presented in Figure 12. The V_{Ag} vacancy was created at the $[AgO_2]$ clusters in the α-$Ag_{2-x}WO_4$ ($x = 0.125$), $Ag_{1-x}O$ ($x = 0.0315$), and $Ag_{2-x}O$ ($x = 0.0625$) models. The V_{Ag} appears in the distorted $[AgO_4]$ clusters in the $Ag_{3-x}O_4$ ($x = 0.125$) system.

Additionally, for comparative purposes, neutral V_O were created, resulting in two remaining electrons that can generate singlet or triplet ground states in the Ag-based oxides. Here, it is important to point out that V_O prefers a singlet configuration in all cases. Therefore, the theoretical calculations indicate that V_O centers do not contribute to the generation of magnetic properties in electron-irradiated Ag-based samples. On the other hand, it is important to control the electronic structure of irradiated Ag-based oxides for the creation of V_O centers. In this case, the band structure and DOS profiles depicted in the Supporting Information (Figure S4) indicate a band-gap reduction for α-Ag_2WO_4 and AgO materials. For Ag_2O and Ag_3O_4, defects act on the vicinity of the band-gap region. This widens the excitation energy due to the enlargement of remaining Ag−O bonds neighboring the V_O center.

Figure 13 displays the calculated band structure and density of state profiles for defective Ag-based oxides. These can be compared with the electronic structure for pristine Ag-base oxides depicted in the Supporting Information (Figure S4).
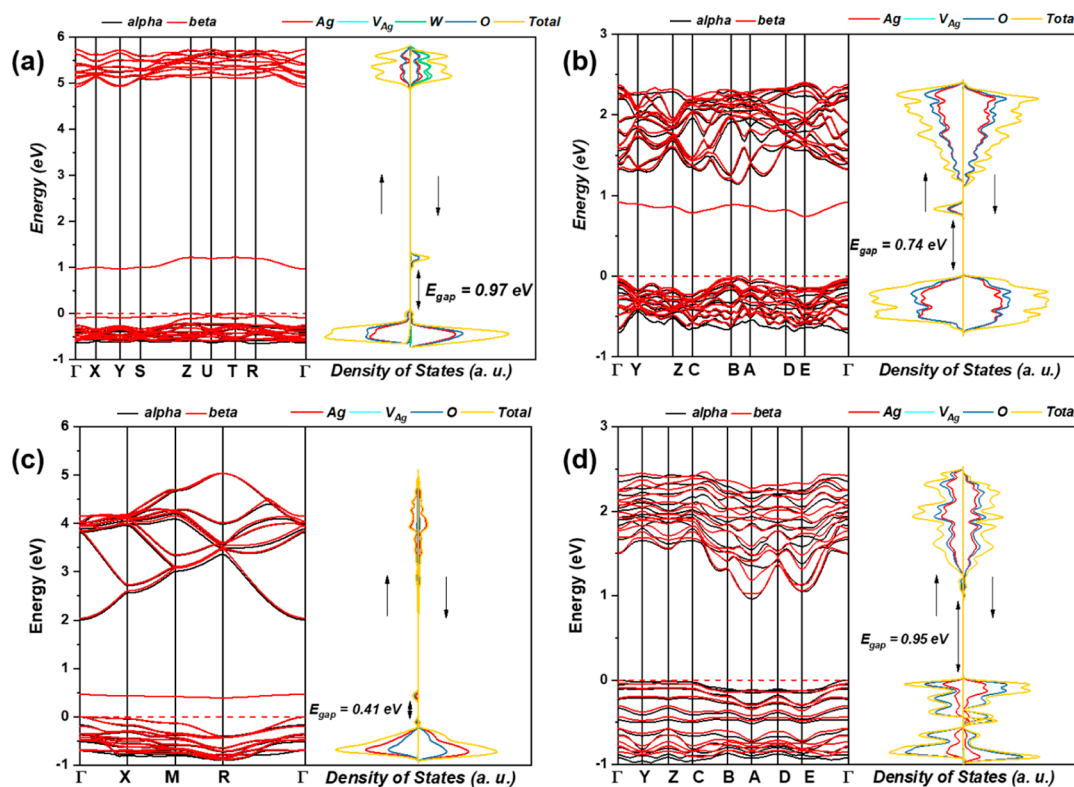
Figure 12. Schematic representation of defective models used for (a) α-Ag$_{2-x}$WO$_4$ (x = 0.125), (b) Ag$_{1-x}$O (x = 0.03125), (c) Ag$_{2-x}$O (x = 0.0625), and (d) Ag$_{3-x}$O$_4$ (x = 0.125) oxides. In reference to α-Ag$_{2-x}$WO$_4$ (a) golden, green, purple, and orange balls correspond to [AgO$_2$], [AgO$_4$], [AgO$_6$], and [AgO$_7$] clusters, respectively. For Ag$_{1-x}$O (b), gray and blue balls correspond to [AgO$_2$] and [AgO$_4$] clusters, respectively. For Ag$_{2-x}$O (c), gray balls present the [AgO$_2$] clusters. In Ag$_{3-x}$O$_4$ (d), the gray and blue balls correspond to distorted and regular [AgO$_4$] clusters, respectively.

Figure 13 presents the energy-level distribution for defective compounds of α-Ag$_{2-x}$WO$_4$, Ag$_{1-x}$O, and Ag$_{2-x}$O (see Figure 13A−C). These are related to the creation of V$_{Ag}$ and the appearance of intermediary energy levels within the band-gap
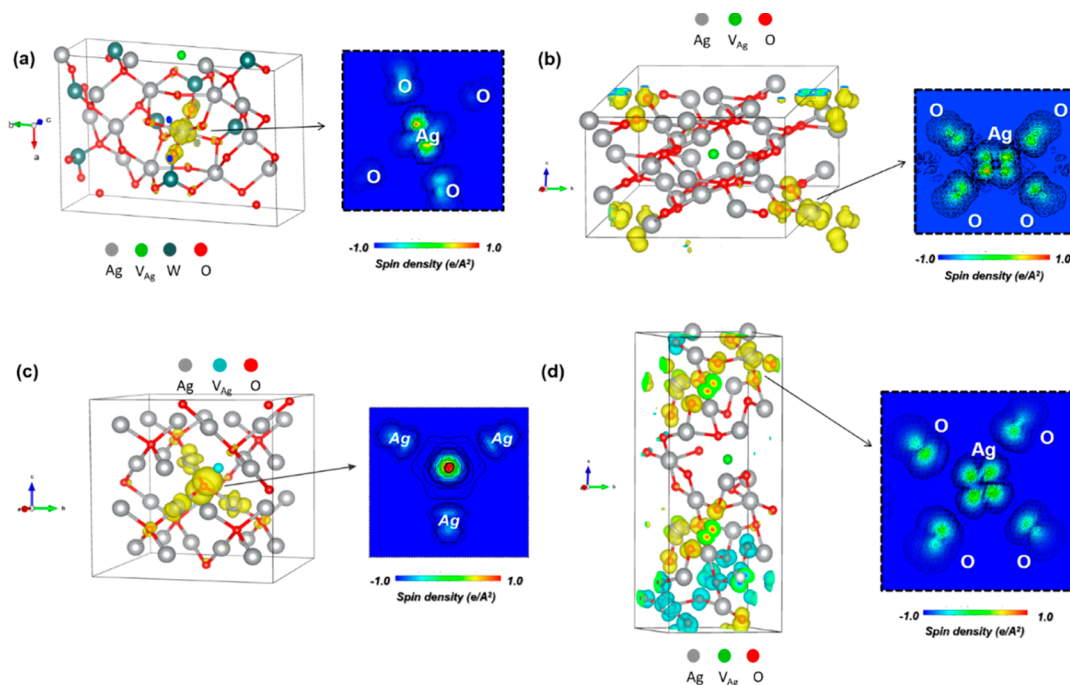
region of pristine oxides (Figures S4A−C). An analysis of the results renders band gap values of 0.41 eV for Ag$_{2-x}$O, 0.74 eV for Ag$_{1-x}$O, and 0.97 eV for α-Ag$_{2-x}$WO$_4$. Additionally, we see the creation of one electronic hole inside the crystalline that exhibits a spin alpha occupation. This was in the vicinity of the Fermi level (VB maximum, VBM) corresponding to bonding electronic states associated with Ag and O atoms, indicating the generation of magnetic Ag species. On the other hand, the opposite spin direction was located within the band-gap region for pristine oxides, generating a new conduction band minimum composed of mixed electronic states of Ag and O atoms. In the opposite direction, the electronic structure for Ag$_{3-x}$O$_4$ (see Figure 13D) shows unusual behavior compared to the pristine structure (see Figure S4D). The pristine electronic structure of Ag$_3$O$_4$ shows metallic character. This is associated with the singlet fundamental state of Ag$^{2+/3+}$ configurations. These results, combined with the Bader charge values, indicate that the Ag$_3$O$_4$ compound is composed of intermediary Ag$^{2+/3+}$ with metallic character. This is in agreement with previous findings. The creation of V$_{Ag}$ centers indicate that hole-induced band separation generates a band-gap value of 0.95 eV. This can be attributed to charge separation of the remaining electronic holes. These holes are spread out along the crystalline structure, generating a singlet configuration.

Figure 14 shows two-dimensional and three-dimensional (2D and 3D) spin isosurfaces for all the models. These models aimed to shed light on spin density distribution in defective Ag-based oxides. The results for Ag$_{2-x}$WO$_4$ (Figure 14A) show that the creation of V$_{Ag}$ centers induces hole-localization in the neighboring clusters, resulting in reduced [AgO$_n$]′ centers that exhibit magnetic Ag species. This is displayed in the spin

Figure 13. Band structure and atom-resolved density of states for defective oxides of (a) α-Ag$_{2-x}$WO$_4$ (x = 0.125), (b) Ag$_{1-x}$O (x = 0.03125), (c) Ag$_{2-x}$O (x = 0.0625), and (d) Ag$_{3-x}$O$_4$ (x = 0.125) oxides.
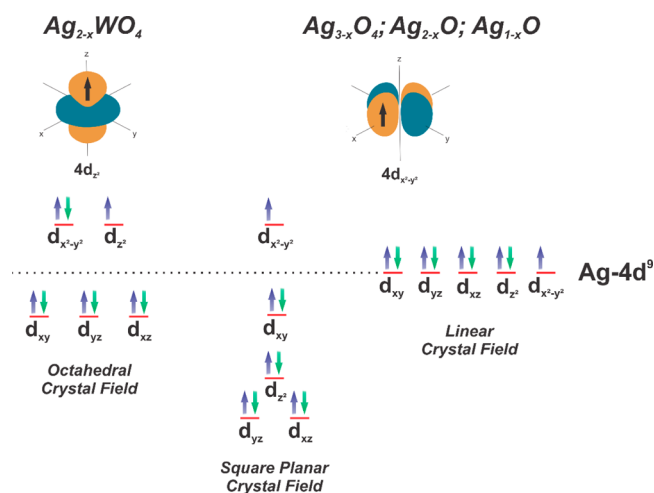
Figure 14. Spin density isosurface and 2D spin density maps for defective oxides (a) α-$Ag_{2-x}WO_4$ ($x = 0.125$), (b) $Ag_{1-x}O$ ($x = 0.03125$), (c) $Ag_{2-x}O$ ($x = 0.0625$), and (d) $Ag_{3-x}O_4$ ($x = 0.125$) oxides. The yellow and blue spin density isosurfaces correspond to α- and β-spin orientations, respectively.

density map for distribution of the unpaired spin in the atomic-like 4_{z^2} orbital. Similar results were obtained from analysis of the other Ag-based oxides. The main changes were associated with the atomic-like $4d_{x^2y^2}$ orbitals of Ag, where the unpaired electron density is located. These observations were attributed to the stronger interaction between these magnetic centers and O anions. These interactions are provoked by structural distortion, charge reduction, and generation of metallic Ag NPs. The latter is responsible for the defective V_{Ag} sites in the crystalline structure of these oxides.

Therefore, using symmetry factors, charge values, and electronic structure analysis, it is possible to argue that EBI of α-Ag_2WO_4 generates magnetic Ag centers via the growth of metallic Ag NPs. This is because it induces the creation of V_{Ag} centers in α-Ag_2WO_4, Ag_3O_4, Ag_2O, and AgO oxides at different concentrations. In an opposite direction, similar concentrations of V_O do not contribute to generate magnetic properties for such oxides, which can be attributed to the stabilization of singlet ground-state for the remaining electrons. Therefore, only defective Ag centers can tailor the magnetic properties of α-Ag_2WO_4, Ag_3O_4, Ag_2O, and AgO oxides.

The local electronic configuration of the Ag cation (the relative energies of the d orbitals and how they are filled) determines the magnetic properties of complex Ag oxides. It defines how many unpaired electrons are present which has a strong influence on which mechanisms the oxides can be involved in.[85,86] The local electronic configuration is, in turn, determined by the oxidation state (the d-electron count), the number of coordinating ligands, and the geometry they adopt around the Ag cation. The electronic structures of octahedral, square planar, and linear $[AgO_n]$ clusters (as determined by crystal field theory) are shown in Figure 15. These have been analyzed and discussed to deduce the origin of magnetic Ag centers.

Figure 15. Schematic representation of crystal field splitting for octahedral, square planar, and linear clusters containing metallic Ag ($4d^9$) centers at α-$Ag_{2-x}WO_4$ ($x = 0.125$), $Ag_{1-x}O$ ($x = 0.03125$), $Ag_{2-x}O$ ($x = 0.0625$), and $Ag_{3-x}O_4$ ($x = 0.125$) oxides. The main orbitals involved in the generation of magnetic Ag centers are highlighted.

In terms of solid-state packing, square-planar coordination is disfavored because it gives rise to shorter anion–anion distances (and thus, increases unfavorable anion–anion repulsion) than the corresponding tetrahedral or linear arrangements. The relative instability of square planar coordination can be considered as a competition between packing efficiency and local electronic stability. Square-planar coordination can be favored over tetrahedral or linear coordination for d^9 electron. The relatively weak ligand-field strength of the oxide ion means that the electronic stability of d^9 square-planar units can generally only overcome the

unfavorable steric/packing factors under the influence of the stronger ligand fields of the heavy 4d orbitals of Ag. On the other hand, the divalent Ag^{2+} cation is unstable in oxidic environments; therefore, it tends to disproportionate into Ag^+/Ag^{3+} combinations, as exemplified by the simple binary oxide AgO.[87]

The presented results demonstrate that oxides of $Ag_{3-x}O_4$, $Ag_{2-x}O$, and $Ag_{1-x}O$ exhibit magnetic Ag centers ($4d^9$), where the unpaired electrons are mainly concentrated along the $4d_{x^2-y^2}$ orbitals. $Ag_{2-x}O$ exhibits linear $[AgO_2]$ clusters in the vicinity of V_{Ag} centers. These act as trapping centers for the remaining spin. In contrast, $Ag_{3-x}O_4$ and $Ag_{1-x}O$ have distorted $[AgO_4]$ clusters neighboring the V_{Ag} centers. This stabilizes the unpaired electron density along the $4d_{x^2-y^2}$ orbitals of the magnetic Ag centers. On the other hand, for the complex structure of α-$Ag_{2-x}WO_4$, the obtained results indicate that $[AgO_6]$ clusters are closely associated with the V_{Ag} center. This results in the localization of unpaired electrons in the z-oriented 4d orbital of Ag. Furthermore, the results presented in Figure 15 explain the isosurfaces depicted in Figure 14. This confirmed the atomic-like character of the orbitals which were involved in the stabilization of the magnetic Ag centers generated from the electron irradiation mechanism.

3. CONCLUSIONS

The pursuit of magnetic behavior in diamagnetic materials has always been difficult, although several efforts have been made to this effect. Herein, we accomplished a breakthrough in that we obtained intrinsic magnetization of α-Ag_2WO_4 under electron beam and FLI. The main conclusions of this work can be summarized as follows: (i) we have demonstrated, for first time, that α-Ag_2WO_4 can be magnetized by electron beam and FLI; (ii) the formation and growth of Ag nanofilaments were observed on the surface of α-Ag_2WO_4 crystals, and the presence of silver oxides (AgO, Ag_2O, and Ag_3O_4) were detected in the composition of an extruded material; (iii) the experimental results were supported by DFT studies, and different scenarios for controlling the magnetic properties were investigated; (iv) the effect of adding electrons to the crystalline structures of α-Ag_2WO_4, Ag_3O_4, Ag_2O, and AgO, and the creation of Ag and O vacancies on these compounds were analyzed; the magnetic activity and structure−activity relationships were rationalized using theoretical analysis; (v) a mechanism was proposed to explain the formation and growth processes of metallic Ag and was also used to explain the appearance of magnetic behavior under EBI; the mechanism was based on structural and electronic changes to the Ag centers in the constituent clusters; (vi) the present results provide a clear overview of the dynamics of Ag NP formation during the synthesis process; and (vii) the controllable magnetic properties of a large-area α-Ag_2WO_4 nanostructure would be an excellent building block, for example, as a spin-polarized electron source at the Fermi level for energy-efficient spintronic devices. The results pave a new avenue for α-Ag_2WO_4-based spintronics applications.

4. EXPERIMENTAL SECTION

4.1. Synthesis. α-Ag_2WO_4 samples were obtained using the co-precipitation method, following our previous study.[58]

4.2. Electron Beam Irradiation. To obtain electron-irradiated α-Ag_2WO_4 (α-Ag_2WO_4:E sample), the synthesized

α-Ag_2WO_4 sample was placed in a field emission gun scanning electron microscope (SEM) for 5 min with an acceleration voltage of 15 kV. A Supra 35-VP instrument (Carl Zeiss, Germany) was used.

4.3. Femtosecond Laser Irradiation. α-Ag_2WO_4 pellets were irradiated with 150 fs pulses (fwhm) from a Ti:sapphire laser (CPA-2001 system from Clark-MXR Inc.). The laser was centered at 780 nm and operated at a repetition rate of 1 kHz. Using a 75 mm focal distance lens, a laser beam (10 mm in diameter with an average power of 200 mW) was focused onto the surface of an α-Ag_2WO_4 pellet. An 8 mm lens was used to center the laser focus in order to obtain the femtosecond laser-irradiated material (α-Ag_2WO_4:F sample). For non-focused samples, where the lens was not used in the irradiation system, the samples have been referred to as non-focused (α-Ag_2WO_4:NF sample).

4.4. Characterization. Samples of α-Ag_2WO_4 were structurally characterized by XRD using a D/Max-2500PC diffractometer (Rigaku, Japan) with Cu Kα radiation (λ = 1.5406 Å) in the 2θ range of 10−70° with a scanning speed of 1° min^{-1} in the Rietveld routine. The Rietveld refinements were performed in the General Structure Analysis System (GSAS) program. Micro-Raman spectra were recorded using an iHR550 spectrometer (HORIBA Jobin-Yvon, Japan) coupled to a CCD detector and an argon-ion laser (Melles Griot, USA) operating at 514.5 nm with a maximum power of 200 mW and a fiber microscope. The morphology, texture, and size of the samples were observed with a field-emission scanning electron microscope (Supra 35-VP, Carl Zeiss, Germany). The microscope was operated at 15 kV. TEM images were obtained by using a Jeol JEM-2100F operating at 200 kV. PL measurements were taken as a function of temperature (15−300 K) using a 500MSpex spectrometer coupled to a GaAs photomultiplier tube (GaAs PMT). A Kimmon He−Cd laser (325 nm laser; 40 mW maximum power) was used as the excitation source for PL measurements. XPS analyses were performed on a Scienta Omicron ESCA spectrometer (Germany) using a monochromatic X-ray source of Al Kα (1486.7 eV). Peak deconvolution was performed using a 70:30% Gaussian−Lorentzian line shape and a Shirley nonlinear sigmoid-type baseline. The binding energies of all elements were calibrated with reference to the C 1s peak at 284.8 eV. Magnetization measurements as a function of applied magnetic field ($M \times H$) and temperature ($M \times T$) were performed using a Quantum Design VSM-SQUID magnetometer. Measurements were taken at temperatures up to 350 K. The zero-field cooling/field cooling (ZFC/FW) procedure was used for $M \times T$ measurements. In all measurements the diamagnetic contribution was subtracted using a linear fitting in $M \times H$ in low and high temperatures.

4.5. Computational Methods and Model Systems. The EBI-induced formation of metallic Ag in α-Ag_2WO_4, Ag_3O_4, Ag_2O, and AgO compounds was studied using first-principles DFT total-energy calculations, as implemented in the VASP program[88,89] using PBE + U,[90] with the Hubbard parameter set to 6.0 eV. The electron−ion interaction was described using project to augmented wave pseudopotentials.[88] The plane-wave expansion was truncated at a cutoff energy of 460 eV, and the Brillouin zones were sampled through 4 × 4 × 4 Monkhorst−Pack special k-point grids. These ensure geometrical and energetic convergence for the Ag-based structures considered in this work. The keyword NELECT was used to increase the number of electrons in the bulk

structure. All crystal structures were simultaneously optimized for their unit cell volumes and atomic positions. The relationship between the charge density topology, molecular structure, and bonding were investigated using the quantum theory of atoms in molecules(QTAIM) developed by Bader.[91,92]

Using the CRYSTAL17 code,[93] the Becke, 3-parameter, Lee−Yang−Parr (B3LYP) hybrid functional[94] has been employed to carefully investigate the magnetic arrangement associated with the creation of Ag and O vacancies in α-Ag_2WO_4, Ag_3O_4, Ag_2O, and AgO oxides. In this case, the unit cells for all Ag-based oxides were built from experimental results for lattice parameters and atomic positions. Full optimizations (cell parameters and atomic coordinates) were carried out on appropriate supercells to simulate the creation of Ag and O vacancies (V_{Ag} and V_O, respectively) on the crystalline structure. The neutral V_{Ag} and V_O centers were modeled by embedding supercells containing 56 atoms for α-Ag_2WO_4 and Ag_3O_4 systems and 48 and 64 atoms for the Ag_2O and AgO systems, respectively. Therefore, Ag-defective systems were described as α-$Ag_{2-x}WO_4$ ($x = 0.125$), $Ag_{1-x}O$ ($x = 0.03125$), $Ag_{2-x}O$ ($x = 0.0625$), and $Ag_{3-x}O_4$ ($x = 0.125$). On the other hand, the O-defective systems can be described as α-Ag_2WO_{4-x} ($x = 0.125$), AgO_{1-x} ($x = 0.03125$), Ag_2O_{1-x} ($x = 0.0625$), and Ag_3O_{4-x} ($x = 0.125$). Previous calculations indicated the most favorable sites for electron-beam induced reduction of Ag centers. These calculations were used to select the atomic positions for creation of V_{Ag} centers.

The Ag and W atoms were described by effective core pseudopotential HAYWSC-311d31G and HAYWSC-11d31G, respectively, while O atoms were described by atom-centered all-electron Gaussian basis 8-411G, respectively. Electronic integration over the BZ was performed using a $4 \times 4 \times 4$ Monkhorst−Pack[95] k-mesh for the pristine and defective cells containing 10 k-points. Five thresholds were set to 8, 8, 8, 8, and 16. These thresholds controlled the accuracy of the Coulomb and exchange integral calculations. The converge criteria for mono electronic and bielectronic integrals were set to 1×10^{-8} hartree, while the root mean square (rms) gradient, rms displacement, maximum gradient, and maximum displacement were set to 3×10^{-4}, 1.2×10^{-3}, 4.5×10^{-4}, and 1.8×10^{-3} a.u., respectively. In our calculations, lattice parameters and atomic positions were relaxed for both pristine and defective models. Electronic properties for all systems were evaluated using the density of states, band structure profiles, and spin density analysis.

ASSOCIATED CONTENT

Ⓢ Supporting Information

The Supporting Information is available free of charge at https://pubs.acs.org/doi/10.1021/acsomega.0c00542.

Auxiliary graphs to understand the differences between α-Ag_2WO_4 samples (Rietveld refinement, XPS survey, connection distances, and band structure) (PDF)

AUTHOR INFORMATION

Corresponding Author

Juan Andrés − *Department of Analytical and Physical Chemistry, University Jaume I (UJI), 12071 Castelló, Spain;* ⓘ orcid.org/0000-0003-0232-3957; Email: andres@qfa.uji.es

Authors

Marcelo Assis − *CDMF, LIEC, Chemistry Department, Federal University of São Carlos—(UFSCar), 13565-905 São Carlos, São Paulo, Brazil;* ⓘ orcid.org/0000-0003-0355-5565

Renan Augusto Pontes Ribeiro − *CDMF, LIEC, Chemistry Department, Federal University of São Carlos—(UFSCar), 13565-905 São Carlos, São Paulo, Brazil;* ⓘ orcid.org/0000-0002-4128-8296

Maria Helena Carvalho − *Physics Department, Federal University of São Carlos—(UFSCar), 13565-905 São Carlos, São Paulo, Brazil*

Mayara Mondego Teixeira − *CDMF, LIEC, Chemistry Department, Federal University of São Carlos—(UFSCar), 13565-905 São Carlos, São Paulo, Brazil;* ⓘ orcid.org/0000-0001-9038-0024

Yara Galvão Gobato − *Physics Department, Federal University of São Carlos—(UFSCar), 13565-905 São Carlos, São Paulo, Brazil*

Gabriela Augusta Prando − *Physics Department, Federal University of São Carlos—(UFSCar), 13565-905 São Carlos, São Paulo, Brazil*

Cleber Renato Mendonça − *IFSC—Instituto de Física de São Carlos, Universidade de São Paulo—(USP), 13566-590 São Carlos, São Paulo, Brazil*

Leonardo de Boni − *IFSC—Instituto de Física de São Carlos, Universidade de São Paulo—(USP), 13566-590 São Carlos, São Paulo, Brazil;* ⓘ orcid.org/0000-0002-1875-1852

Adilson Jesus Aparecido de Oliveira − *Physics Department, Federal University of São Carlos—(UFSCar), 13565-905 São Carlos, São Paulo, Brazil*

Jefferson Bettini − *Brazilian Nanotechnology National Laboratory (LNNano), BR-13083100 Campinas, São Paulo, Brazil*

Elson Longo − *CDMF, LIEC, Chemistry Department, Federal University of São Carlos—(UFSCar), 13565-905 São Carlos, São Paulo, Brazil;* ⓘ orcid.org/0000-0001-8062-7791

Complete contact information is available at: https://pubs.acs.org/10.1021/acsomega.0c00542

Notes

ACKNOWLEDGMENTS

REFERENCES

(1) Trudel, S. Unexpected Magnetism in Gold Nanostructures: Making Gold Even More Attractive. *Gold Bull.* **2011**, *44*, 3−13.

(2) Nealon, G. L.; Donnio, B.; Greget, R.; Kappler, J.-P.; Terazzi, E.; Gallani, J.-L. Magnetism in Gold Nanoparticles. *Nanoscale* **2012**, *4*, 5244−5258.

(3) Sundaresan, A.; Bhargavi, R.; Rangarajan, N.; Siddesh, U.; Rao, C. N. R. Ferromagnetism as a Universal Feature of Nanoparticles of the Otherwise Nonmagnetic Oxides. *Phys. Rev. B: Condens. Matter Mater. Phys.* **2006**, *74*, 161306.

(4) Garitaonandia, J. S.; Insausti, M.; Goikolea, E.; Suzuki, M.; Cashion, J. D.; Kawamura, N.; Ohsawa, H.; Gil de Muro, I.; Suzuki, K.; Plazaola, F.; et al. Chemically Induced Permanent Magnetism in Au, Ag, and Cu Nanoparticles: Localization of the Magnetism by Element Selective Techniques. *Nano Lett.* **2008**, *8*, 661−667.

(5) Armelao, L.; Barreca, D.; Bottaro, G.; Gasparotto, A.; Gross, S.; Maragno, C.; Tondello, E. Recent Trends on Nanocomposites Based on Cu, Ag and Au Clusters: A Closer Look. *Coord. Chem. Rev.* **2006**, *250*, 1294−1314.

(6) Sargolzaei, M.; Lotfizadeh, N. Spin and Orbital Magnetism of a Single 3d Transition-Metal Atom Doped into Icosahedral Coinage-Metal Clusters X 12 (X=Cu, Ag, Au). *Phys. Rev. B: Condens. Matter Mater. Phys.* **2011**, *83*, 155404.

(7) Marenco, A. J.; Pedersen, D. B.; Trudel, S. On the Origin of the Ferromagnetic Signature in Silver Nanoparticles and Thin Films. *J. Mater. Chem. C* **2017**, *5*, 4899−4908.

(8) Haynes, W. M.; Lide, D. R.; Bruno, T. J. *CRC Handbook of Chemistry and Physics: A Ready-Reference Book of Chemical and Physical Data*, 96th ed.; CRC Press: Boca Raton, FL, 2016.

(9) Landrum, G. A.; Dronskowski, R. The Orbital Origins of Magnetism: From Atoms to Molecules to Ferromagnetic Alloys. *Angew. Chem. Int. Ed.* **2010**, *31*, 1560.

(10) Venkatesan, M.; Fitzgerald, C. B.; Coey, J. M. D. Unexpected Magnetism in a Dielectric Oxide. *Nature* **2004**, *430*, 630.

(11) Carvalho, M. H.; Rizzo Piton, M.; Lemine, O. M.; Bououdina, M.; Galeti, H. V. A.; Souto, S.; Pereira, E. C.; Galvão Gobato, Y.; de Oliveira, A. J. A. Effects of Strain, Defects and Crystal Phase Transition in Mechanically Milled Nanocrystalline In_2O_3 Powder. *Mater. Res. Express* **2018**, *6*, 025017.

(12) Coey, J. M. D.; Venkatesan, M.; Stamenov, P.; Fitzgerald, C. B.; Dorneles, L. S. Magnetism in Hafnium Dioxide. *Phys. Rev. B: Condens. Matter Mater. Phys.* **2005**, *72*, 3−4.

(13) Hong, N. H.; Sakai, J.; Poirot, N.; Brizé, V. Room-Temperature Ferromagnetism Observed in Undoped Semiconducting and Insulating Oxide Thin Films. *Phys. Rev. B: Condens. Matter Mater. Phys.* **2006**, *73*, 132404.

(14) Wang, H.; Zong, Z.; Yan, Y. Mechanism of Multi-Defect Induced Ferromagnetism in Undoped Rutile TiO_2. *J. Appl. Phys.* **2014**, *115*, 233909.

(15) Li, J.; Jiang, Y.; Li, Y.; Yang, D.; Xu, Y.; Yan, M. Origin of Room Temperature Ferromagnetism in MgO Films. *Appl. Phys. Lett.* **2013**, *102*, 072406.

(16) Qin, H.; Zhang, Z.; Liu, X.; Zhang, Y.; Hu, J. Room-Temperature Ferromagnetism in CuO Sol−Gel Powders and Films. *J. Magn. Magn Mater.* **2010**, *322*, 1994−1998.

(17) Aravindh, S. D. A.; Schwingenschloegl, U.; Roqan, I. S. Defect Induced d 0 Ferromagnetism in a ZnO Grain Boundary. *J. Chem. Phys.* **2015**, *143*, 224703.

(18) Chang, G. S.; Forrest, J.; Kurmaev, E. Z.; Morozovska, A. N.; Glinchuk, M. D.; McLeod, J. A.; Moewes, A.; Surkova, T. P.; Hong, N. H. Oxygen-Vacancy-Induced Ferromagnetism in Undoped SnO_2 Thin Films. *Phys. Rev. B: Condens. Matter Mater. Phys.* **2012**, *85*, 165319.

(19) Fernandes, V.; Mossanek, R. J. O.; Schio, P.; Klein, J. J.; de Oliveira, A. J. A.; Ortiz, W. A.; Mattoso, N.; Varalda, J.; Schreiner, W. H.; Abbate, M.; et al. Dilute-Defect Magnetism: Origin of Magnetism in Nanocrystalline CeO_2. *Phys. Rev. B: Condens. Matter Mater. Phys.* **2009**, *80*, 35202.

(20) Hu, J.; Zhang, Z.; Zhao, M.; Qin, H.; Jiang, M. Room-Temperature Ferromagnetism in MgO Nanocrystalline Powders. *Appl. Phys. Lett.* **2008**, *93*, 192503.

(21) Liang, S.; Zhou, J.; Pan, A.; Zhang, X.; Tang, Y.; Tan, X.; Chen, T.; Wu, R. Facile Synthesis of $Ag/AgVO_3$ Hybrid Nanorods with Enhanced Electrochemical Performance as Cathode Material for Lithium Batteries. *J. Power Sources* **2013**, *228*, 178−184.

(22) Beltrán, J. I.; Monty, C.; Balcells, L.; Martínez-Boubeta, C. Possible D^0 Ferromagnetism in MgO. *Solid State Commun.* **2009**, *149*, 1654−1657.

(23) Kumar, N.; Sanyal, D.; Sundaresan, A. Defect Induced Ferromagnetism in MgO Nanoparticles Studied by Opticaland Positron Annihilation Spectroscopy. *Chem. Phys. Lett.* **2009**, *477*, 360−364.

(24) Araujo, C. M.; Kapilashrami, M.; Jun, X.; Jayakumar, O. D.; Nagar, S.; Wu, Y.; Århammar, C.; Johansson, B.; Belova, L.; Ahuja, R.; et al. Room Temperature Ferromagnetism in Pristine MgO Thin Films. *Appl. Phys. Lett.* **2010**, *96*, 232505.

(25) Elfimov, I. S.; Yunoki, S.; Sawatzky, G. A. Possible Path to a New Class of Ferromagnetic and Half-Metallic Ferromagnetic Materials. *Phys. Rev. Lett.* **2002**, *89*, 216403.

(26) Osorio-Guillén, J.; Lany, S.; Barabash, S. V.; Zunger, A. Magnetism without Magnetic Ions: Percolation, Exchange, and Formation Energies of Magnetism-Promoting Intrinsic Defects in CaO. *Phys. Rev. Lett.* **2006**, *96*, 107203.

(27) Chanier, T.; Opahle, I.; Sargolzaei, M.; Hayn, R.; Lannoo, M. Magnetic State around Cation Vacancies in II-VI Semiconductors. *Phys. Rev. Lett.* **2008**, *100*, 026405.

(28) Das Pemmaraju, C.; Sanvito, S. Ferromagnetism Driven by Intrinsic Point Defects in HfO_2. *Phys. Rev. Lett.* **2005**, *94*, 217205.

(29) Rahman, G.; García-Suárez, V. M.; Hong, S. C. Vacancy-Induced Magnetism in SnO_2: A Density Functional Study. *Phys. Rev. B: Condens. Matter Mater. Phys.* **2008**, *78*, 184404.

(30) Gao, F.; Hu, J.; Yang, C.; Zheng, Y.; Qin, H.; Sun, L.; Kong, X.; Jiang, M. First-Principles Study of Magnetism Driven by Intrinsic Defects in MgO. *Solid State Commun.* **2009**, *149*, 855−858.

(31) Wang, F.; Pang, Z.; Lin, L.; Fang, S.; Dai, Y.; Han, S. Magnetism in Undoped MgO Studied by Density Functional Theory. *Phys. Rev. B: Condens. Matter Mater. Phys.* **2009**, *80*, 144424.

(32) Mahadevan, P.; Mahalakshmi, S. Suitability of p -Type Conditions for Ferromagnetism in GaN:Mn. *Phys. Rev. B: Condens. Matter Mater. Phys.* **2006**, *73*, 153201.

(33) Dev, P.; Xue, Y.; Zhang, P. Defect-Induced Intrinsic Magnetism in Wide-Gap III Nitrides. *Phys. Rev. Lett.* **2008**, *100*, 117204.

(34) Larson, P.; Satpathy, S. Effect of Vacancies on Ferromagnetism in GaN:Mn Dilute Magnetic Semiconductors from First-Principles. *Phys. Rev. B: Condens. Matter Mater. Phys.* **2007**, *76*, 245205.

(35) Yan, T.; Ye, N.; Xu, L.; Sang, Y.; Chen, Y.; Song, W.; Long, X.; Wang, J.; Liu, H. Ferromagnetism in Chemically Reduced $LiNbO_3$ and $LiTaO_3$ Crystals. *J. Phys. D: Appl. Phys.* **2016**, *49*, 195005.

(36) Cao, E.; Zhang, Y.; Qin, H.; Zhang, L.; Hu, J. Vacancy-Induced Magnetism in Ferroelectric $LiNbO_3$ and $LiTaO_3$. *Phys. B* **2013**, *410*, 68−73.

(37) Wang, B.-Y.; Zhang, G.-Y.; Cui, G.-W.; Xu, Y.-Y.; Liu, Y.; Xing, C.-Y. Controllable Fabrication of α-Ag_2WO4 Nanorod-Clusters with Superior Simulated Sunlight Photocatalytic Performance. *Inorg. Chem. Front.* **2019**, *6*, 209−219.

(38) Assis, M.; Robeldo, T.; Foggi, C. C.; Kubo, A. M.; Mínguez-Vega, G.; Condoncillo, E.; Beltran-Mir, H.; Torres-Mendieta, R.; Andrés, J.; Oliva, M.; et al. Ag Nanoparticles/α-Ag_2WO_4 Composite Formed by Electron Beam and Femtosecond Irradiation as Potent Antifungal and Antitumor Agents. *Sci. Rep.* **2019**, *9*, 9927.

(39) Roca, R. A.; Sczancoski, J. C.; Nogueira, I. C.; Fabbro, M. T.; Alves, H. C.; Gracia, L.; Santos, L. P. S.; de Sousa, C. P.; Andrés, J.; Luz, G. E.; et al. Facet-Dependent Photocatalytic and Antibacterial Properties of α-Ag_2WO_4 Crystals: Combining Experimental Data and Theoretical Insights. *Catal. Sci. Technol.* **2015**, *5*, 4091−4107.

(40) Guo, C.-X.; Yu, B.; Xie, J.-N.; He, L.-N. Silver Tungstate: A Single-Component Bifunctional Catalyst for Carboxylation of Terminal Alkynes with CO_2 in Ambient Conditions. *Green Chem.* **2015**, *17*, 474−479.

(41) Chen, H.; Xu, Y. Photoactivity and Stability of Ag_2WO_4 for Organic Degradation in Aqueous Suspensions. *Appl. Surf. Sci.* **2014**, *319*, 319−323.

(42) Longo, E.; Volanti, D. P.; Longo, V. M.; Gracia, L.; Nogueira, I. C.; Almeida, M. A. P.; Pinheiro, A. N.; Ferrer, M. M.; Cavalcante, L. S.; Andrés, J. Toward an Understanding of the Growth of Ag Filaments on á-Ag_2WO_4 and Their Photoluminescent Properties: A Combined Experimental and Theoretical Study. *J. Phys. Chem. C* **2014**, *118*, 1229−1239.

(43) Andrés, J.; Gracia, L.; Gonzalez-Navarrete, P.; Longo, V. M.; Avansi, W., Jr.; Volanti, D. P.; Ferrer, M. M.; Lemos, P. S.; La Porta, F. A.; Hernandes, A. C.; et al. Structural and Electronic Analysis of the Atomic Scale Nucleation of Ag on α-Ag_2WO_4 Induced by Electron Irradiation. *Sci. Rep.* **2014**, *4*, 5391.

(44) da Silva, L. F.; Catto, A. C.; Avansi, W.; Cavalcante, L. S.; Mastelaro, V. R.; Andrés, J.; Aguir, K.; Longo, E. Acetone Gas Sensor Based on α-Ag_2WO_4 Nanorods Obtained via a Microwave-Assisted Hydrothermal Route. *J. Alloys Compd.* **2016**, *683*, 186−190.

(45) Pereira, W. d. S.; Andrés, J.; Gracia, L.; San-Miguel, M. A.; da Silva, E. Z.; Longo, E.; Longo, V. M. Elucidating the Real-Time Ag Nanoparticle Growth on α-Ag_2WO_4 during Electron Beam Irradiation: Experimental Evidence and Theoretical Insights. *Phys. Chem. Chem. Phys.* **2015**, *17*, 5352−5359.

(46) Zhang, X.-Y.; Wang, J.-D.; Liu, J.-K.; Yang, X.-H.; Lu, Y. Construction of Silver Tungstate Multilevel Sphere Clusters by Controlling the Energy Distribution on the Crystal Surface. *CrystEngComm* **2015**, *17*, 1129−1138.

(47) Vafaeezadeh, M.; Mahmoodi Hashemi, M. One Pot Oxidative Cleavage of Cyclohexene to Adipic Acid Using Silver Tungstate Nano-Rods in a Brønsted Acidic Ionic Liquid. *RSC Adv.* **2015**, *5*, 31298−31302.

(48) Xiang, Q.; Yu, J.; Jaroniec, M. Synergetic Effect of MoS_2 and Graphene as Cocatalysts for Enhanced Photocatalytic H_2 Production Activity of TiO_2 Nanoparticles. *J. Am. Chem. Soc.* **2012**, *134*, 6575−6578.

(49) Kako, T.; Kikugawa, N.; Ye, J. Photocatalytic Activities of $AgSbO_3$ under Visible Light Irradiation. *Catal. Today* **2008**, *131*, 197−202.

(50) Jin, R.; Zeng, C.; Zhou, M.; Chen, Y. Atomically Precise Colloidal Metal Nanoclusters and Nanoparticles: Fundamentals and Opportunities. *Chem. Rev.* **2016**, *116*, 10346−10413.

(51) Chakraborty, I.; Pradeep, T. Atomically Precise Clusters of Noble Metals: Emerging Link between Atoms and Nanoparticles. *Chem. Rev.* **2017**, *117*, 8208−8271.

(52) Longo, E.; Volanti, D. P.; Longo, V. M.; Gracia, L.; Nogueira, I. C.; Almeida, M. A. P.; Pinheiro, A. N.; Ferrer, M. M.; Cavalcante, L. S.; Andrés, J. Toward an Understanding of the Growth of Ag Filaments on α-Ag_2WO_4 and Their Photoluminescent Properties: A Combined Experimental and Theoretical Study. *J. Phys. Chem. C* **2014**, *118*, 1229−1239.

(53) Pereira, W. d. S.; Andrés, J.; Gracia, L.; San-Miguel, M. A.; da Silva, E. Z.; Longo, E.; Longo, V. M. Elucidating the Real-Time Ag Nanoparticle Growth on α-Ag_2WO_4 during Electron Beam Irradiation: Experimental Evidence and Theoretical Insights. *Phys. Chem. Chem. Phys.* **2015**, *17*, 5352−5359.

(54) Roca, R. A.; Gouveia, A. F.; Lemos, P. S.; Gracia, L.; Andrés, J.; Longo, E. Formation of Ag Nanoparticles on β-Ag_2WO_4 through Electron Beam Irradiation: A Synergetic Computational and Experimental Study. *Inorg. Chem.* **2016**, *55*, 8661−8671.

(55) Fabbro, M. T.; Saliby, C.; Rios, L. R.; La Porta, F. A.; Gracia, L.; Li, M. S.; Andrés, J.; Santos, L. P. S.; Longo, E. Identifying and Rationalizing the Morphological, Structural, and Optical Properties of β-Ag_2MoO_4 Microcrystals, and the Formation Process of Ag Nanoparticles on Their Surfaces: Combining Experimental Data and First-Principles Calculations. *Sci. Technol. Adv. Mater.* **2015**, *16*, 065002.

(56) Andrés, J.; Ferrer, M. M.; Gracia, L.; Beltran, A.; Longo, V. M.; Cruvinel, G. H.; Tranquilin, R. L.; Longo, E. A Combined Experimental and Theoretical Study on the Formation of Ag Filaments on β-Ag_2MoO_4 Induced by Electron Irradiation. *Part. Part. Syst. Char.* **2015**, *32*, 646−651.

(57) Botelho, G.; Sczancoski, J. C.; Andres, J.; Gracia, L.; Longo, E. Experimental and Theoretical Study on the Structure, Optical Properties, and Growth of Metallic Silver Nanostructures in Ag_3PO_4. *J. Phys. Chem. C* **2015**, *119*, 6293−6306.

(58) Assis, M.; Cordoncillo, E.; Torres-Mendieta, R.; Beltrán-Mir, H.; Mínguez-Vega, G.; Oliveira, R.; Leite, E. R.; Foggi, C. C.; Vergani, C. E.; Longo, E.; et al. Towards the Scale-up of the Formation of Nanoparticles on α-Ag_2WO_4 with Bactericidal Properties by Femtosecond Laser Irradiation. *Sci. Rep.* **2018**, *8*, 1−11.

(59) Sczancoski, J. C.; Maya-Johson, S.; Da Silva Pereira, W.; Longo, E.; Leite, E. R. Atomic Diffusion Induced by Electron-Beam Irradiation: An in Situ Study of Ag Structures Grown from α-Ag_2WO_4. *Cryst. Growth Des.* **2019**, *19*, 106−115.

(60) Cavalcante, L. S.; Almeida, M. A. P.; Avansi, W.; Tranquilin, R. L.; Longo, E.; Batista, N. C.; Mastelaro, V. R.; Li, M. S. Cluster Coordination and Photoluminescence Properties of α-Ag_2WO_4 Microcrystals. *Inorg. Chem.* **2012**, *51*, 10675−10687.

(61) Thompson, P.; Cox, D. E.; Hastings, J. B. Rietveld Refinement of Deybe-Scherrer Synchrotron X-Ray Data from Al_2O_3. *J. Appl. Crystallogr.* **1987**, *20*, 79−83.

(62) Finger, L. W.; Cox, D. E.; Jephcoat, A. P. A Correction for Powder Diffraction Peak Asymmetry Due to Axial Divergence. *J. Appl. Crystallogr.* **1994**, *27*, 892−900.

(63) Stephens, P. W. Phenomenological Model of Anisotropic Peak Broadening in Powder Diffraction. *J. Appl. Crystallogr.* **1999**, *32*, 281−289.

(64) Turkovič, A.; Fox, D. L.; Scott, J. F.; Geller, S.; Ruse, G. F. High Temperature Raman Spectroscopy of Silver Tetratungstate, $Ag_8W_4O_{16}$. *Mater. Res. Bull.* **1977**, *12*, 189−195.

(65) Longo, V. M.; De Foggi, C. C.; Ferrer, M. M.; Gouveia, A. F.; André, R. S.; Avansi, W.; Vergani, C. E.; Machado, A. L.; Andrés, J.; Cavalcante, L. S.; et al. Potentiated Electron Transference in α-Ag_2WO_4 Microcrystals with Ag Nanofilaments as Microbial Agent. *J. Phys. Chem. A* **2014**, *118*, 5769−5778.

(66) De Foggi, C. C.; De Oliveira, R. C.; Fabbro, M. T.; Vergani, C. E.; Andres, J.; Longo, E.; Machado, A. L. Tuning the Morphological, Optical, and Antimicrobial Properties of α-Ag_2WO_4 Microcrystals Using Different Solvents. *Cryst. Growth Des.* **2017**, *17*, 6239−6246.

(67) Macedo, N. G.; Gouveia, A. F.; Roca, R. A.; Assis, M.; Gracia, L.; Andrés, J.; Leite, E. R.; Longo, E. Surfactant-Mediated Morphology and Photocatalytic Activity of α-Ag_2WO_4 Material. *J. Phys. Chem. C* **2018**, *122*, 8667−8679.

(68) Andrés, J.; Gracia, L.; Gonzalez-Navarrete, P.; Longo, V. M.; Avansi, W.; Volanti, D. P.; Ferrer, M. M.; Lemos, P. S.; La Porta, F. A.; Hernandes, A. C.; et al. Structural and Electronic Analysis of the Atomic Scale Nucleation of Ag on α-Ag_2WO_4 Induced by Electron Irradiation. *Sci. Rep.* **2014**, *4*, 5391.

(69) San-Miguel, M. A.; Da Silva, E. Z.; Zanetti, S. M.; Cilense, M.; Fabbro, M. T.; Gracia, L.; Andrés, J.; Longo, E. In Situ Growth of Ag Nanoparticles on α-Ag_2WO_4 under Electron Irradiation: Probing the Physical Principles. *Nanotechnology* **2016**, *27*, 225703.

(70) Spreadborough, J.; Christian, J. W. High-temperature X-ray diffractometer. *J. Sci. Instrum.* **1959**, *36*, 116−118.

(71) Novgorodova, M. I.; Gorshkov, A. I.; Mokhov, A. V. Native Silver and its New Structural Modifications. *Int. Geol. Rev.* **1981**, *23*, 485−494.

(72) Macedo, N. G.; Machado, T. R.; Roca, R. A.; Assis, M.; Foggi, c. C.; Puerto-Belda, V.; Mínguez-Vega, G.; Rodrigues, A.; San-Miguel, M. A.; Cordoncillo, E.; Beltrán-Mir, H.; Andrés, J.; Longo, E. Tailoring the Bactericidal Activity of Ag Nanoparticles/α-Ag_2WO_4 Composite Induced by Electron Beam and Femtosecond Laser Irradiation: Integration of Experiment and Computational Modeling. *ACS Appl. Bio Mater.* **2019**, *2*, 824−837.

(73) Urbanová, M.; Pokorná, D.; Bakardjieva, S.; Šubrt, J.; Bastl, Z.; Bezdička, P.; Pola, J. IR Laser-Induced Ablation of Ag in Dielectric Breakdown of Gaseous Hydrocarbons: Simultaneous Occurrence of

Metastable hcp and Stable fcc Ag Nanostructures in C:H Shell. *J. Photochem. Photobiol., A* **2010**, *213*, 114−122.

(74) Murzakaev, A. M. Size Dependence of the Phase Composition of Silver Nanoparticles Formed by the Electric Explosion of a Wire. *Phys. Met. Metallogr.* **2017**, *118*, 459−465.

(75) Assis, M.; Carvalho De Oliveira, M.; Machado, T. R.; Macedo, N. G.; Costa, J. P. C.; Gracia, L.; Andrés, J.; Longo, E. In Situ Growth of Bi Nanoparticles on NaBiO₃ , *δ*-, and *β*-Bi₂O₃ Surfaces: Electron Irradiation and Theoretical Insights. *J. Phys. Chem. C* **2019**, *123*, 5023−5030.

(76) Trench, A. B.; Machado, T. R.; Gouveia, A. F.; Assis, M.; da Trindade, L. G.; Santos, C.; Perrin, A.; Perrin, C.; Oliva, M.; Andrés, J.; et al. Connecting Structural, Optical, and Electronic Properties and Photocatalytic Activity of Ag₃PO₄ :Mo Complemented by DFT Calculations. *Appl. Catal., B* **2018**, *238*, 198−211.

(77) He, H.; Xue, S.; Wu, Z.; Yu, C.; Yang, K.; Peng, G.; Zhou, W.; Li, D. Sonochemical Fabrication, Characterization and Enhanced Photocatalytic Performance of Ag₂S/Ag₂WO₄ Composite Microrods. *Chin. J. Catal.* **2016**, *37*, 1841−1850.

(78) Xie, F. Y.; Gong, L.; Liu, X.; Tao, Y. T.; Zhang, W. H.; Chen, S. H.; Meng, H.; Chen, J. XPS Studies on Surface Reduction of Tungsten Oxide Nanowire Film by Ar⁺ Bombardment. *J. Electron Spectrosc. Relat. Phenom.* **2012**, *185*, 112−118.

(79) Tang, J.; Ye, J. Correlation of Crystal Structures and Electronic Structures and Photocatalytic Properties of the W-Containing Oxides. *J. Mater. Chem.* **2005**, *15*, 4246−4251.

(80) Tang, J.; Zou, Z.; Ye, J. Photophysical and Photocatalytic Properties of AgInW₂O₈. *J. Phys. Chem. B* **2003**, *107*, 14265−14269.

(81) A, S.; P, P. K.; K, B. K.; S, G.; Varghese, T. Influence of Electron Beam Irradiation on Structural and Optical Properties of Alpha Ag₂WO₄. *Micron* **2016**, *88*, 1−6.

(82) Zhang, F.; Yiu, Y.; Aronson, M. C.; Wong, S. S. Exploring the Room-Temperature Synthesis and Properties of Multifunctional Doped Tungstate Nanorods. *J. Phys. Chem. C* **2008**, *112*, 14816−14824.

(83) Longo, V. M.; Figueiredo, A. T. d.; Campos, A. B.; Espinosa, J. W. M.; Hernandes, A. C.; Taft, C. A.; Sambrano, J. R.; Varela, J. A.; Longo, E. Different Origins of Green-Light Photoluminescence Emission in Structurally Ordered and Disordered Powders of Calcium Molybdate. *J. Phys. Chem. A* **2008**, *112*, 8920−8928.

(84) Kröger, F. A.; Vink, H. J. Relations between the Concentrations of Imperfections in Crystalline Solids. *Solid State Phys.* **1956**, *3*, 307−435.

(85) Goodenough, J. B. *Magnetism and the Chemical Bond*; Elsevier B.V.: New York, 1963.

(86) Gerloch, M.; Constable, E. C. *Transition Metal Chemistry: The Valence Shell in the d-Block*; Wiley: Weinheim, 1994.

(87) Greenwood, N. N.; Earnshaw, A. *Chemistry of the Elements*; Elsevier B.V.: Oxford, 1997.

(88) Kresse, G.; Furthmüller, J. Efficiency of Ab-Initio Total Energy Calculations for Metals and Semiconductors Using a Plane-Wave Basis Set. *Comput. Mater. Sci.* **1996**, *6*, 15−50.

(89) Kresse, G.; Hafner, J. Ab Initio Molecular-Dynamics Simulation of the Liquid-Metal−Amorphous-Semiconductor Transition in Germanium. *Phys. Rev. B: Condens. Matter Mater. Phys.* **1994**, *49*, 14251−14269.

(90) Perdew, J. P.; Burke, K.; Ernzerhof, M. Quantum Theory Group Tulane University, N. O. L. 70118 J. Generalized Gradient Approximation Made Simple. *Phys. Rev. Lett.* **1996**, *77*, 3865−3868.

(91) Popelier, P. L. A.; Aicken, F. M.; O'brien, S. E. *Chemical Modelling: Applications and Theory*; Elsevier Ltd: Hinchliffe, 2000; Vol. *1*.

(92) Bader, R. F. W. *Atoms in Molecules—A Quantum Theory*; Oxford University Press: Oxford, U.K., 1990.

(93) Dovesi, R.; Erba, A.; Orlando, R.; Zicovich-Wilson, C. M.; Civalleri, B.; Maschio, L.; Rérat, M.; Casassa, S.; Baima, J.; Salustro, S.; et al. Quantum-Mechanical Condensed Matter Simulations with CRYSTAL. *Wiley Interdiscip. Rev.: Comput. Mol. Sci.* **2018**, *8*, No. e1360.

(94) Becke, A. D. Density-Functional Thermochemistry III. The Role of Exact Exchange. *J. Chem. Phys.* **1993**, *98*, 5648−5652.

(95) Monkhorst, H. J.; Pack, J. D. Special Points Fro Brillouin-Zone Integretions. *Phys. Rev. B: Solid State* **1976**, *13*, 5188−5192.